

1 **DATA-DRIVEN RECONSTRUCTION AND ENCODING OF SPARSE
2 STIMULI ACROSS CONVERGENT SENSORY LAYERS FROM
3 DOWNSTREAM NEURONAL NETWORK DYNAMICS***

4 VICTOR J. BARRANCA[†], YOLANDA HU[†], ZOE POTERFIELD[†], SAMUEL ROTHSTEIN[†],
5 AND ALEX XUAN[†]

6 **Abstract.** Neuronal networks vary dramatically in size, connectivity structure, and function-
7 ality across downstream layers of the brain. This raises the question of whether information is lost
8 as it is re-encoded along compressive and expansive pathways. In this work, we develop a poten-
9 tial *data-driven* mechanism for the preservation of information in the activity of neuronal networks
10 across downstream layers, which uses the widespread linearity of individual neuronal responses to
11 sufficiently strong ramped artificial inputs to fit a linear input-output mapping across the network.
12 We analyze the dynamics of several families of two-layer neuronal network models, where the input
13 components far outnumber the downstream neurons as in compressive pathways, and apply the fitted
14 mapping in conjunction with compressive sensing theory to reconstruct stimuli with sparse structure.
15 The input-output mapping facilitates stimulus reconstructions that only use measurements of down-
16 stream neuronal firing rates in response to inputs over a short time duration, furnishing stimulus
17 recovery even when theoretical analysis is intractable or the governing equations of the dynamical sys-
18 tem are unknown as in experiment. Similarly accurate stimulus reconstructions are obtained across
19 different single-neuron models, network coupling functions, and image classes. Improved reconstruc-
20 tions are yielded when uniformly-random feedforward connectivity is replaced by spatially localized
21 feedforward connectivity akin to receptive fields. We expect similar principles could be leveraged
22 experimentally in prosthetics as well as in the reconstruction of large-scale network connectivity.

23 **Key words.** Neuronal network dynamics, Signal processing, Input-output mappings

24 **AMS subject classifications.** 92C42, 92C05, 37N25, 94A08

25 **1. Introduction.** As stimuli are processed in sensory systems, information is
26 encoded in the dynamics of neuronal networks of disparate sizes and connectivity
27 structures. Across downstream layers in the brain, an especially common feature in
28 feedforward connectivity is compression and subsequent re-expansion. In the early
29 human visual system, for example, compression occurs when a stimulus injected into
30 a network of approximately 150 million photoreceptors is subsequently processed by
31 only roughly 1.5 million retinal ganglion cells. Further downstream, information en-
32 coded by the millions of neurons in the Lateral Geniculate Nucleus (LGN) is later ex-
33 panded when re-encoded by the primary visual cortex, which contains approximately
34 40 times as many neurons as the LGN [10, 103]. Similarly, the human olfactory system
35 begins with about 15 million olfactory receptor neurons that feed into just thousands
36 of glomeruli before re-expansion into a network of millions of neurons in the piriform
37 cortex [121, 118, 92, 86, 102]. This structure has been observed in various auditory
38 and somatosensory systems as well [105, 75, 80, 26], and is therefore hypothesized to
39 be central to efficient coding in the brain [9, 8, 68].

40 Numerous functional benefits to compression and re-expansion have been pro-
41 posed and verified theoretically [56, 4]. In the resultant low-dimensional space after
42 compression, neuronal networks have the potential to perform redundancy reduction,
43 prune extraneous sensory data, and facilitate especially rapid information processing

*Submitted to the editors DATE.

Funding: This work was supported by NSF grant DMS-1812478 and a Swarthmore Faculty Research Support Grant.

[†]Department of Mathematics and Statistics, Swarthmore College, Swarthmore, PA (vbarran1@swarthmore.edu, <http://www.swarthmore.edu/NatSci/vbarran1/>).

[71, 124]. Compression onto smaller neuronal networks via parallel pooling may also enhance robustness to noise and improve performance in learning as well as classification tasks [22, 84, 38, 41]. Nonetheless, if not performed intelligently, such massive compression could result in destructive information loss. What potential mechanisms may preserve information across sensory bottlenecks and how are stimuli embedded in the dynamics of low-dimensional neuronal networks?

Previous work has largely investigated this question in the context of learned stimulus representations or highly idealized neuronal network models. Through unsupervised learning, for instance, sparse representations of sets of sub-sampled stimuli can be developed without knowing the sampling structure or sparse basis for the stimuli, but such a framework does not fully address how reconstructions may be obtained without learning or in the context of realistic neuronal network activity [40]. Other approaches leverage linear or discrete-time dynamics to encode sparse sequences of information in the network dynamics, but they do not address the more realistic case of continuous and nonlinear network dynamics [55]. Recent work in the context of simple spiking neuronal network models with nonlinear dynamics has successfully reconstructed natural scenes using measurements of evoked firing rates; however, this line of research requires knowledge of the underlying dynamical equations governing the network activity for a successful reconstruction, which is likely not available to neurons in the brain or in experiments [17, 16, 21].

In this work, we investigate the reconstruction and encoding of stimuli from evoked nonlinear neuronal network dynamics *without* knowledge of the underlying governing equations. We develop a new *data-driven* framework for the recovery of realistic inputs into two-layer neuronal network models by leveraging the ubiquitous linearity of neuronal responses to sufficiently strong stimuli [117, 96, 81]. Using the evoked downstream neuronal activity across the network for a small set of ramped artificial inputs, we first construct an approximate linear input-output mapping intrinsic to the nonlinear network dynamics. With the resultant highly underdetermined linear system reflecting a sensory bottleneck, we use the widespread sparsity of natural stimuli in combination with compressive sensing (CS) theory to reconstruct novel gray-scale natural scene inputs from the evoked downstream neuronal dynamics and thereby gauge the accuracy of input encoding [52, 36]. When using sufficiently unstructured measurements of sparse signals, CS theory facilitates successful reconstructions with a dramatic reduction in sampling rate as compared to classical uniform sampling [100], potentially enabling the preservation of stimulus information across convergent network layers.

We show that this encoding and reconstruction framework is successful for a host of models with varying levels of biological realism, including both current-based and conductance-based integrate-and-fire (I&F) single neuron models [31, 101, 77, 37] and networks with either pulse-coupling or alpha-function coupling between downstream neurons [91, 69, 33, 43]. For alternative inputs, such as Poisson spike train inputs with image-based drive strengths and color image inputs, we also produce successful reconstructions based on the evoked network dynamics. When the uniformly random feedforward connectivity is adapted to reflect the spatial localization common in visual receptive fields, our framework yields improved stimulus reconstructions as expected from the evolutionary selection of sensory system structure.

This work provides a possible mechanism for information preservation across the common compressive and expansive pathways in the brain, which is robust to different modeling choices and is fundamentally consistent with many key physiological observations. Regardless of whether this particular mechanism is utilized by the brain, we

94 nevertheless provide a proof of concept for the retention of signals across neuronal
 95 networks of widely varying sizes. It also lays a possible groundwork for important
 96 extensions to large-scale network connectivity reconstructions and improved design of
 97 sensory prosthetic devices.

98 The remainder of the paper is structured as follows. In Sect. 2, we introduce
 99 the two-layer network model with a downstream compressive layer that we will study
 100 throughout this work, beginning in the context of current-based I&F dynamics with
 101 pulse-coupling between downstream neurons. We then develop our data-driven net-
 102 work input-output mapping approximation methodology in Sect. 3 and subsequent
 103 CS input recovery framework in Sect. 4. To gauge the encoding properties of the
 104 network, here we analyze sample stimulus reconstructions as well as study their ro-
 105 bustness to limitations in the measurement data and noise. We show how this input
 106 encoding mechanism generalizes to alternative stimulus types in Sect. 5 and extends
 107 to more detailed neuronal network models in Sect. 6. Finally, we investigate the
 108 impact of the feedforward connectivity structure in Sect. 7 and discuss implications
 109 as well as natural extensions of this work in Sect. 8.

110 **2. Two-Layer Network Model with Current-Based Integrate-And-Fire**
 111 **Neuronal Dynamics.** To investigate information encoding along compressive path-
 112 ways, we use the framework of a two-layer feedforward network, consisting of a sensory
 113 input layer that transmits the incoming stimulus and a downstream output layer that
 114 encodes the stimulus through its nonlinear neuronal dynamics. We model compressive
 115 encoding across sensory layers of disparate sizes by assuming that the input layer has
 116 significantly more components than the output layer, typically differing by a factor of
 117 ten throughout this work.

118 Our initial analysis will assume that the downstream layer is governed by the
 119 dynamics of a pulse-coupled integrate-and-fire neuronal network driven by the input
 120 layer signal [31, 91, 101, 32, 88]. The I&F model well reproduces experimentally
 121 recorded subthreshold membrane potential dynamics and firing statistics, and it pos-
 122 sses the additional benefit of furnishing relatively computationally inexpensive sim-
 123 ulations [1, 96, 116, 15]. For concreteness, we will utilize the current-based I&F model
 124 in this section and we will later generalize our framework to the conductance-based
 125 setting in Sect. 6.1.

126 The membrane potential dynamics of the i^{th} neuron in the downstream layer are
 127 governed by

$$128 \quad (2.1) \quad \frac{dv_i}{dt} = -(v_i - V_R) + \sum_{j=1}^n F_{ij} p_j + \frac{S}{N_R} \sum_{\substack{k=1 \\ k \neq i}}^m R_{ik} \sum_l \delta(t - \tau_{kl}),$$

129 evolving from the resting voltage V_R until reaching firing threshold voltage V_T . At
 130 this moment, the neuron fires (spikes), and its voltage is immediately reset to V_R . At
 131 the time of the l^{th} spike of the k^{th} neuron, τ_{kl} , instantaneous inputs $(S/N_R)\delta(t - \tau_{kl})$
 132 are injected into all post-connected (post-synaptic) neurons in the downstream layer,
 133 where $\delta(\cdot)$ is the Dirac delta function, S is the recurrent connection strength, and N_R
 134 is the number of recurrent connections. This pulse-coupling reflects the extremely
 135 short time scale of each firing event, and in Sect. 6.2 we will consider impact of
 136 finite-time interactions between the downstream neurons.

137 With respect to the network connectivity structure, we assume m and n are the
 138 numbers of downstream I&F neurons and input layer components, respectively, with
 139 $n \gg m$ to reflect the compressive layer. The feed-forward connection (adjacency)

140 matrix between the two network layers is $F = (F_{ij})$; we say that the i^{th} neuron in the
 141 downstream layer is post-connected to the j^{th} input component if $F_{ij} \neq 0$. For con-
 142 creteness, we assume here that the input components randomly and sparsely feed into
 143 each downstream neuron, such that each possible feedforward connection is equally
 144 probable and each realized connection in F has equal strength, f . In Sect. 7, we will
 145 examine the impact of alternative and more realistic feedforward connectivity struc-
 146 ture. The constant vector $p = (p_1, \dots, p_n)$ gives the stimulus component strengths
 147 transmitted by the upstream layer neurons, which will be generated by the pixels in
 148 an n -component gray-scale image. Since photoreceptors in the early visual system, for
 149 example, are known to undergo graded potentials with responses indicative of local
 150 light intensities, we initially model the feedforward input from the initial layer as fixed
 151 in time [108]. Later, in Sect. 5, we will consider the cases of color image inputs and
 152 spiking inputs from the upstream layer.

153 The downstream recurrent connectivity matrix is similarly given by $R = (R_{ij})$.
 154 We assume the probability of a connection is low for both connectivity matrices, gen-
 155 erating sparse feed-forward and recurrent connections as often found in experiment
 156 [87, 57, 62]. For generality, we assume the downstream neurons are connected, but
 157 we can also assume that they are uncoupled without impacting our overall analysis
 158 by setting $R_{ij} = 0$ for all i, j [15, 11]. While ganglion cells in the retina, for example,
 159 are in some studies measured to be disconnected, there are other cases in which con-
 160 nectivity is observed and yet other scenarios where gap junctions are found between
 161 neurons [44, 111, 109]. This modeling framework is meant to capture the essence of
 162 compressive sensory pathways and potential frameworks for successful data compres-
 163 sion in neuronal dynamics rather than reflecting the specifics found in any one sensory
 164 system in a particular organism.

165 Unless specified otherwise, we choose $n = 10000$ input layer neurons, $m = 1000$
 166 downstream neurons, feedforward connection probability $1/m = 0.001$, and the recur-
 167 rent connection probability 0.05. We also select nondimensional parameters $V_R = 0$,
 168 $V_T = 1$, and $t = 1$ to correspond to a time-scale of 20ms, as typically produced in
 169 nondimensionalization [90, 17, 28]. We generally simulate the time evolution of this
 170 model over $0 \leq t \leq 10$, which is comparable to typical human reaction times of 200ms
 171 [2, 3].

172 **3. Data-Driven Network Input-Output Map Fitting.** The issues posed by
 173 the encoding of input layer stimuli in the dynamics of the neurons in the downstream
 174 layer are two-fold. First, since the pathway is compressive, the inverse problem of
 175 recovering the large number of input components from measurements of a relatively
 176 small number of downstream neurons is highly underdetermined. Second, the down-
 177 stream neuronal dynamics are nonlinear and vary in time, making the direct applica-
 178 tion of linear recovery techniques infeasible.

179 To address this second problem, previous work had considered the limit of a
 180 large downstream network size with high neuronal firing rates and small recurrent
 181 communication strength, with coarse-graining techniques analogous to kinetic theory
 182 in nonequilibrium statistical mechanics yielding an approximate network input-output
 183 mapping [110, 34, 18, 12, 11]. In the Appendix, we include a brief derivation of this
 184 approximate *theoretical* input-output mapping for the current-based integrate-and-fire
 185 neuronal network as well as a comparison with the data-driven mapping discussed
 186 in detail throughout the remainder of this section. This theoretical input-output
 187 relationship is static in time and linear, relating the downstream neuronal firing rate
 188 vector $\mu = (\mu_1, \dots, \mu_m)$ measured from simulation to the injected stimulus vector p

189 via

190 (3.1)
$$\mu = \frac{Fp}{(V_T - V_R)} - \frac{e_m}{2} + \frac{S}{N_R(V_T - V_R)} R\mu,$$

191 where e_m is an m -vector of ones.192 However, analytically deriving such a theoretical mapping is not feasible for more
193 detailed neuronal network models and it is not clear how to obtain an input-output
194 mapping when the underlying equations governing the neuronal dynamics are un-
195 known. To deal with these issues, in this work we instead take a data-driven approach
196 in obtaining such an input-output relationship. We inject into the network a small
197 number of artificial random stimuli, $p^{(1)}, \dots, p^{(r)}$, ramping up the mean strength of
198 each by adjusting the feedforward connectivity scaling constant f . For each input, we
199 record the resultant firing rate vectors, $\mu^{(1)}, \dots, \mu^{(r)}$, across the downstream neuronal
200 network.201 In Fig. 1 (a), we consider the firing rate response for an individual representative
202 downstream neuron in our model across an ensemble of ramped external inputs. We
203 depict the firing rate as a function of the external input scaling strength, which is a
204 multiplicative factor scaling the generated input stimuli. We see that for sufficiently
205 strong stimulation strengths, the firing rate increases in a highly linear fashion. This is
206 also true for each of the other individual downstream neuronal firing rates as well as for
207 the network-averaged firing rate, though the detailed structure of each curve may vary
208 from neuron to neuron. The linearity of neuronal gain curves is well documented in
209 the context of more realistic neuronal models in many dynamical regimes, including
210 the Exponential Integrate-And-Fire and Hodgkin-Huxley models, as well as in the
211 presence of realistic ionic currents [30, 54, 15, 117]. Experimental recordings have
212 similarly exhibited a linear increase in response with scaled external inputs [117, 96,
213 81]. Overall, the shape of the gain curve here resembles that of Rectified Linear Units
214 (ReLUs), which are especially effective and common in machine learning applications
215 [82]. If additional biological features are included in the single neuron dynamics, such
216 as a refractory period following action potentials [76, 15], a more sigmoidal gain curve
217 may be obtained, which will still generally have an accurate linear approximation for
218 a broad range of stimulus strengths.219 While the resultant firing rate response may vary from neuron to neuron, we can
220 approximate a linear input-output mapping for the i^{th} downstream neuron by

221 (3.2)
$$\mu_i = \alpha_i(Fp)_i + \beta_i,$$

222 where α_i and β_i are constants produced from a least-squares linear fit of form (3.2) to
223 the firing rate responses of the i^{th} neuron, $\mu_i^{(1)}, \dots, \mu_i^{(r)}$, across the ramped external
224 inputs, $p^{(1)}, \dots, p^{(r)}$, in the linear regime of the gain curve. An example of this fitted
225 linear mapping for the previously considered sample neuron is given in Fig. 1 (a).
226 Across all individual neurons in the downstream layer, the collection of these linear
227 maps yields the *data-driven network linear input-output relationship*.

228 (3.3)
$$\mu = \alpha \odot (Fp) + \beta,$$

229 where \odot denotes entry-wise vector multiplication, $\alpha = (\alpha_1, \dots, \alpha_m)$, and
230 $\beta = (\beta_1, \dots, \beta_m)$. We call α the *slope* coefficients and β the *intercept* coefficients,
231 corresponding to the parameters for the lines fitted to the respective gain curves of
232 the downstream neurons in the linear dynamical regime.

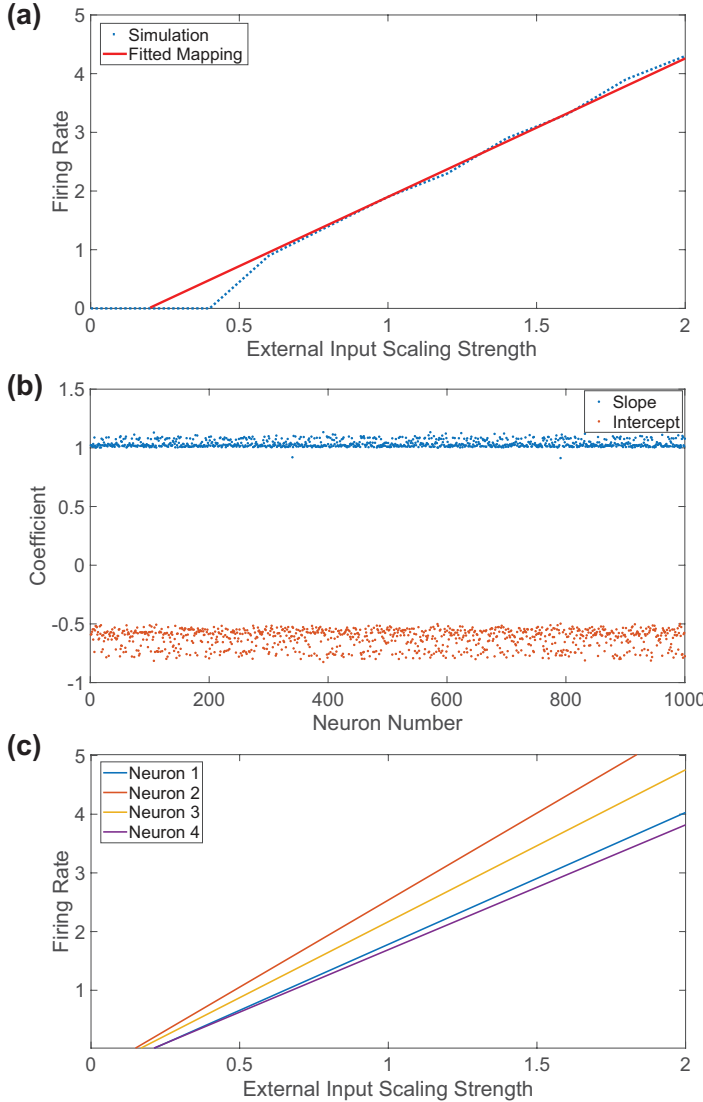


FIG. 1. (a) Gain curve for an individual representative downstream neuron in the two-layer network with current-based neuronal dynamics prescribed by Eq. (2.1), depicting the individual neuronal firing rate as a function of the external input scaling strength across several simulations with ramped constant external inputs (blue). The input-output mapping for that individual neuron is fitted in the linear regime of the gain curve (red). (b) Slope (blue) and intercept (red) coefficients in the data-driven network input-output mapping given by Eq. (3.3) fitted for each downstream neuron in the two-layer network considered in (a). (c) Fitted linear input-output mappings for several additional sample neurons.

233 For this particular idealized two-layer network model, we may validate the data-
 234 driven mapping by direct comparison with the known theoretical input-output rela-
 235 tionship in Eq. (3.1). The slope and intercept coefficients fitted across the down-
 236 stream neuronal network are plotted in Fig. 1 (b). Comparing the results obtained
 237 from Eq. (3.3) to the theoretical input-output map derived via coarse-graining given
 238 by Eq. (3.1), we see close agreement since the α components are clustered around

239 $\alpha \approx \frac{1}{(V_T - V_R)} = 1$ and the β components are clustered around $\beta \approx -\frac{1}{2}$.

240 It is important to underline that the data-driven framework for deriving the net-
 241 work input-output map (3.3) does not require knowledge of the governing model
 242 dynamical system given by Eq. (2.1). In the particular gain curve considered in Fig.
 243 1, each random vector in the input ensemble is initially generated with mean 2, and
 244 to construct different points in the gain curve, each input vector is then multiplied by
 245 a distinct external input scaling strength in $[0, 2]$, with 0.2 spacing between scaling
 246 strengths. The activity of the downstream neurons in response to each given input
 247 vector is recorded over $0 \leq t \leq 10$ to compute the neuronal firing rates used in fitting
 248 each individual neuronal input-output mapping. Although there are some minor dis-
 249 crepancies, the linear regime in the gain curve is about the same for all neurons, and
 250 using only the random input vectors with mean strength of at least 1 in the fitting
 251 process will generally produce an effective network mapping.

252 As discussed in more detail in the next section, this methodology succeeds with
 253 only a small number of ramped input vectors, i.e., 2 or 3 in practice, and for a broad
 254 range of external input strengths, so long as these inputs are sufficiently strong such
 255 that the firing rate gain is approximately linear. There is generally little variability in
 256 the fitted coefficients with the choice of random input vectors utilized. This is to be
 257 expected because for a given downstream neuron, the mapping coefficients obtained
 258 from different stimulus choices will typically vary no more than the coefficients differ
 259 from neuron to neuron across the network as displayed in Fig. 1 (b), since the random
 260 differences in the feed-forward connectivity matrix rows mediate random variations in
 261 net external input across the downstream neurons. The fitted input-output mappings
 262 for several additional downstream neurons are plotted in Fig. 1 (c) for comparison,
 263 demonstrating relatively little variability across the network.

264 We note that it is also possible to fit a linear input-output map that uses data
 265 regarding the time-averaged voltages across the downstream layer, $\bar{v}^{(1)}, \dots, \bar{v}^{(r)}$, cor-
 266 responding to the respective ramped inputs for models or dynamical regimes in which
 267 this data produces a more robust linear mapping of form $\mu = \alpha \odot (Fp) + \beta + \gamma \odot \bar{v}$,
 268 with the additional fitted parameter vector γ [20]. For network dynamics governed
 269 by Eq. (2.1), however, we have verified that including the voltage term does not alter
 270 the encoding capability of the mapping.

271 **4. Stimulus Encoding Across Compressive Layers and Compressive**
 272 **Sensing Reconstructions.** In characterizing a potential mechanism through which
 273 stimulus information may be successfully encoded in downstream neuronal network
 274 dynamics across compressive pathways, we seek to show that it is possible to recon-
 275 struct stimulus information from our model network activity. In particular, we aim
 276 to use the evoked firing rates of the downstream neurons, given by μ , to recover an
 277 input vector with realistic stimulus structure, p , driving the I&F neuronal network
 278 dynamics. The error in the resultant reconstruction of the input, p^{recon} , will then be
 279 used to assess the accuracy of the stimulus encoding in the downstream layer activity.

280 With the approximate input-output mapping that is fitted in Eq. (3.3), we have
 281 a linear relationship between p and μ . However, to reconstruct p from μ requires
 282 solving the related linear system

283 (4.1)
$$Fp = \frac{1}{\alpha} \odot \mu - \frac{1}{\alpha} \odot \beta$$

284 for unknown vector p , where $\frac{1}{\alpha} = \left(\frac{1}{\alpha_1}, \dots, \frac{1}{\alpha_m} \right)$. This system is highly underde-
 285 termined since the feedforward pathway is compressive and thus $m \ll n$. Such a

286 problem generally has infinitely many solutions, yet our goal is to robustly recover
 287 the particular solution corresponding to the true injected input vector p .

288 To address this issue, our reconstruction framework leverages the typical sparsity
 289 of natural stimuli to utilize compressive sensing theory. Natural scenes and sounds
 290 are both sparse in frequency-based domains and odors are sparse in the sense that
 291 they are generally composed of a small number of molecule types [52, 114, 83, 123,
 292 64]. For band-limited signals that are sparse in at least a single domain, CS theory
 293 demonstrates that, in the sparse domain, the number of nonzero components, rather
 294 than the full signal bandwidth [100], determines the minimum sampling rate needed
 295 for an accurate reconstruction [35, 46]. In the case of natural scenes, p is typically
 296 not sparse in the original spatial domain but $\hat{p} = Tp$ is indeed sparse after applying
 297 a sparsifying transform T , such as the discrete cosine or Fourier transform [63, 47].
 298 Upon recovering \hat{p} , the sparsifying transform is then inverted to yield p in the original
 299 domain.

300 Since the sparsest solution to Eq. (4.1) well reconciles a small number of samples,
 301 a natural way to select \hat{p} is to seek the solution with the smallest number of nonzero
 302 components in the sparse domain. However, this approach is typically not possible to
 303 implement in polynomial time, and therefore a more efficient method is desirable [29].
 304 For sufficiently sparse \hat{p} and a broad class of measurement matrices, CS theory shows
 305 that a viable alternative is minimizing $|\hat{p}|_{\ell_1} = \sum_{i=1}^n |\hat{p}_i|$ subject to Eq. (4.1) [36]. This
 306 ℓ_1 optimization problem can be efficiently solved in polynomial time using numerous
 307 numerical methods [112, 47].

308 Measurement matrices suitable for CS are generally simple to generate, with a
 309 large class of matrices with sufficient randomness, such as those with independent,
 310 identically distributed random elements, are proven to satisfy sufficient conditions
 311 for accurate recovery [7]. We note that our feedforward connectivity matrix F well
 312 satisfies these conditions, and we show in Sect. 7 that even when spatial localization,
 313 akin to spatial receptive field structure, is incorporated, CS reconstructions are still
 314 highly accurate and in fact often improved.

315 To reconstruct a gray-scale image input with vectorization $p = (p_1, \dots, p_n)$, we use
 316 the two-dimensional discrete cosine transform (2D-DCT) to sparsify the image. We
 317 note that for one-dimensional stimuli, such as sound waves, we need only consider a
 318 one dimensional transform, and for signal representations of stimuli, such as odorants,
 319 that are sparse in their sampled domain, no transforms are necessary.

320 The $\sqrt{n} \times \sqrt{n}$ 1D-DCT matrix, D , is defined to have entries $D_{ij} = (D^{-1})_{ij}^T =$
 321 $\omega(i) \cos\left(\frac{(i-1)(2j-1)\pi}{2\sqrt{n}}\right)$, where $\omega(1) = (1/n)^{1/4}$ and $\omega(i) = (4/n)^{1/4}$ for $i \neq 1$. The
 322 2D-DCT of an image with vectorization p is $(D \otimes D)p$, where \otimes denotes the $n \times n$
 323 Kronecker product defined such that

$$324 \quad D \otimes D = \begin{bmatrix} D_{11}D & \cdots & D_{1\sqrt{n}}D \\ \vdots & \ddots & \vdots \\ D_{\sqrt{n}1}D & \cdots & D_{\sqrt{n}\sqrt{n}}D \end{bmatrix}.$$

325 Given a vectorized input image, to recover the vectorization of its 2D-DCT, \hat{p} , we
 326 rewrite Eq. (4.1) with respect to the 2D-DCT as

$$327 \quad (4.2) \quad \sum_{j=1}^n F_{ij}(D \otimes D)_{ij}^{-1} \hat{p}_j = \frac{1}{\alpha} \odot \mu - \frac{1}{\alpha} \odot \beta.$$

328 Considering \hat{p} is sparse, upon measuring the evoked neuronal firing rates, μ , we de-
 329 termine the solution to Eq. (4.2) that minimizes $\sum_{j=1}^n |\hat{p}_j|$ to obtain \hat{p} [35, 46]. To
 330 finally reconstruct the stimulus in the spatial domain, p , we invert the 2D-DCT and
 331 the vectorization.

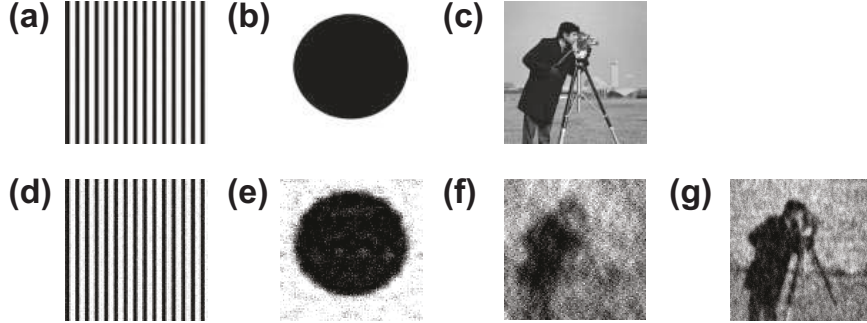


FIG. 2. (a)-(c): Gray-scale input image stimuli composed of 100×100 pixels. (d)-(f): Corresponding CS reconstructions of images in (a)-(c), respectively, using Eq. (4.2) and the data-driven network input-output mapping. The relative reconstruction errors for (d)-(f) are 0.0624, 0.2201, and 0.3092, respectively. (g) Reconstruction of the 250×250 pixel version of image (c) with relative reconstruction error 0.2588. Each CS reconstruction in (d)-(g) uses a factor of 10 less downstream I&F neurons than input pixels with current-based neuronal dynamics prescribed by Eq. (2.1).

332 Several representative gray-scale image reconstructions using this CS recovery
 333 framework in conjunction with the data-driven network input-output mapping are
 334 depicted in Fig. 2. To quantify the accuracy of each stimulus reconstruction, p^{recon} ,
 335 we measure the relative reconstruction error, $\|p - p^{recon}\|/\|p\|$, using the Euclidean
 336 norm, $\|p\| = \sqrt{\sum_i p_i^2}$. We view this error as a measure of information loss along
 337 the compressive layer, though the resultant reconstruction may alternatively be inter-
 338 preted as the stimulus information encoded by the subsequent expansive downstream
 339 layer following compression.

340 For the simpler images in Fig. 2 (a)-(b), we see that the reconstruction is highly
 341 accurate even when there are 10 times as many input pixels as downstream neurons,
 342 akin to a compressive sensory pathway. For the more complicated cameraman image
 343 in Fig. 2 (c), higher error is incurred, but the large-scale features are still well captured
 344 and the reconstruction is recognizable. We use this more detailed natural scene as
 345 our test stimulus in the subsequent analyses, focusing primarily on 100×100 pixel
 346 inputs for computational tractability. The reconstructions obtained using the data-
 347 driven input-output mapping, given by Eq. (3.3), are comparable to those analogously
 348 obtained via the theoretical mapping, given by Eq. (3.1), but since such theoretical
 349 mappings are not feasible to derive for the more detailed models discussed in the
 350 following sections, the data-driven approach developed in this work is a necessity.

351 It is important to emphasize that for higher resolution images with more pixels
 352 and generally more sparsity in the frequency domain, it is possible to reconstruct ad-
 353 ditional, less dominant, image details using the same ratio of downstream to upstream
 354 neurons. In Fig. 2 (g), we consider the cameraman image as in Fig. 2 (c) but instead
 355 with 250×250 pixels while preserving the compression factor so that there is still a
 356 factor of 10 less downstream neurons (i.e., here $m = 6250$ and $n = 62500$). In this
 357 higher resolution case, closer to true sensory system layers with potentially millions
 358 of neurons, we indeed observe an improved and quite accurate reconstruction.

359 While the previous reconstructions used the evoked downstream neuronal firing

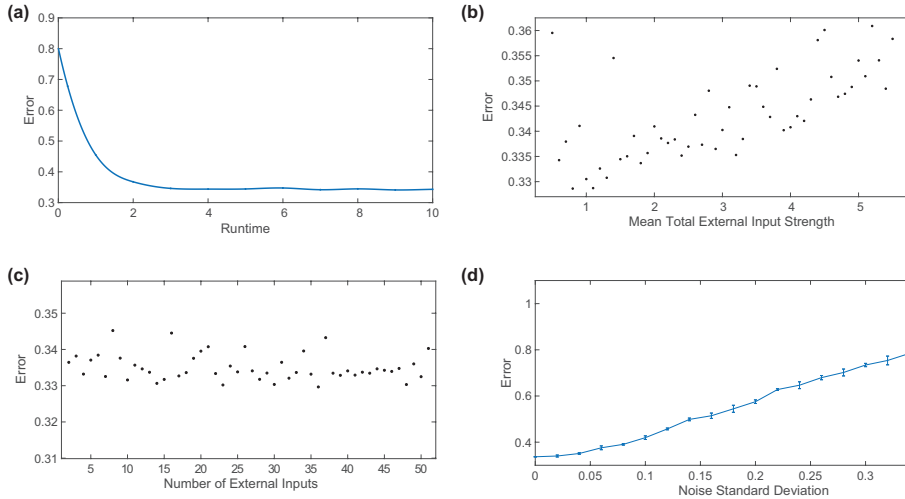


FIG. 3. (a) Relative reconstruction error as a function of the amount of time over which the network dynamics prescribed by Eq. (2.1) are recorded. (b) Relative reconstruction error as a function of the mean external input strength into the downstream neuronal network. For each data point, the error plotted uses data driven mapping (3.3) fitted with 11 different external inputs with strengths centered around the mean strength and strength increments of 0.1. (c) Relative reconstruction error as a function of the number of ramped external inputs used to fit Eq. (3.3). For each data point, the mean external input strength is 2.5 with strengths equally spaced in [1, 4] and centered around the mean. (d) Relative reconstruction error as a function of the standard deviation of the mean 0 Gaussian noise multiplying the recorded downstream neuronal firing rates used in the CS reconstruction. The mean relative reconstruction error is plotted over 5 realizations with error bars giving the standard deviation in the error across noise realizations. For (a)-(d), each panel considers the CS reconstruction of the image in Fig. 2 (c) utilizing a factor of 10 less downstream neurons than pixels and the linear system given by Eq. (4.2).

360 rates recorded over $0 \leq t \leq 10$ each, the reconstruction error generally decreases
 361 with observation time. In Fig. 3 (a), we depict the relative reconstruction error for
 362 the image in Fig. 2 (c) as a function of the simulation runtime, demonstrating a
 363 rapid initial decrease in error that later remains nearly constant for sufficiently long
 364 simulations, i.e., after approximately $t = 2$ or 40ms. Hence, the downstream neuronal
 365 dynamics in the compressive layer may reliably encode stimulus information over a
 366 short and biologically realistic time scale.

367 With regard to fitting the network input-output mapping, the resultant map is
 368 quite insensitive to changes in the number of external inputs used and their strengths.
 369 In Fig. 3 (b), we plot the relative reconstruction error using different linear map fit-
 370 tings, where each mapping is obtained using the same number of ramped input vectors
 371 but different mean input vector strengths. Here we see that as long as the downstream
 372 neuronal dynamics are in the linear regime, the accuracy of the resultant reconstruc-
 373 tion is insignificantly impacted by perturbations in the mean input strength used for
 374 obtaining the data-driven mapping. Varying the mean input vector strength by a
 375 factor of four only results in about 0.02 fluctuations in reconstruction error. Likewise,
 376 if we instead hold the mean input vector strength constant in the linear dynamical
 377 regime but adjust the number of ramped inputs used, as in Fig. 3 (c), the recon-
 378 struction error remains approximately constant so long as at least two input vectors
 379 of distinct strengths are used. The ability to successfully reconstruct detailed stimuli
 380 using data-driven mappings constructed from a small number of artificial inputs over

381 a broad range of input strengths underlines both the efficiency and robustness of this
 382 methodology.

383 Reflecting the potential noise in the response of downstream neurons to stimuli, for
 384 example due to fluctuations in photon absorption, synaptic release, and neurotrans-
 385 mitter availability [49, 76], we consider how information encoding in this framework is
 386 impacted by noise in the downstream neuronal firing rates. To include multiplicative
 387 noise, we multiply each downstream neuronal firing rate obtained from simulation by
 388 a distinct independent, identically distributed Gaussian random variable with mean
 389 0 and standard deviation σ . We use mean 0 noise based on the assumption that the
 390 firing rate fluctuations have no general upward or downward bias. In Figure 3 (d), we
 391 plot the relative reconstruction error as a function of the standard deviation σ and ob-
 392 serve an approximately linear increase in error with σ . Even when the noise standard
 393 deviation is 10% of the firing threshold, the reconstruction error is only increased by
 394 about 15%. For each choice of σ , the reconstruction accuracy is nearly constant across
 395 multiple noise realizations, highlighting the strong stability of information encoding
 396 in neuronal dynamics across compressive pathways.

397 **5. Extensions to Alternative Families of Stimuli.**

398 **5.1. Poisson Spike Train Inputs with Image-Based Drive Strengths.** To
 399 consider alternative forms of compressive pathways, we first adapt our framework to
 400 two-layer networks in which feedforward signals are communicated via spike trains
 401 rather than graded potentials. In this case, the constant input n -vector is replaced
 402 by n Poisson spike trains, reflecting the notion that the time distribution of a large
 403 number of spikes received by any given neuron across a large neuronal network is often
 404 well approximated by event times generated via a Poisson process [119, 6]. The total
 405 mean strengths of the Poisson spike train inputs received by the downstream neurons
 406 are determined by the respective components of the constant vector originally injected,
 407 namely F_p . In particular, the instantaneous membrane potential jump induced by
 408 each feedforward spike from the initial layer is assumed to be held fixed at γ for each
 409 downstream neuron and the corresponding rate for the Poisson input is $(F_p)_i/\gamma$ for
 410 the i^{th} downstream neuron; this neuron is thus driven by a Poisson spike train with
 411 mean drive strength $(F_p)_i$ and its dynamics are determined by Eq. (2.1) aside from
 412 the feedforward input modification. Unless specified otherwise, we select the jump
 413 strength to be $\gamma = 0.01$.

414 As shown in Fig. 4 (a), the individual downstream neuronal firing rate responses
 415 to Poisson spike train inputs with ramped mean drive strengths are highly linear for
 416 sufficiently large drive strengths. In the limit of high incoming Poisson spike train
 417 rates and low induced voltage jumps with fixed mean drive strength F_p across the
 418 downstream neurons, the drive from the initial layer approaches the original constant
 419 input vector [39]. Thus, we use the same methodology as described in Sect. 3 to fit
 420 the data-driven input-output mapping across the downstream layer, except now we do
 421 this via ramped artificial spike train inputs with their respective mean drive strengths
 422 neighboring the slope coefficients in Eq. (3.3). The resultant coefficients in the data-
 423 driven network input-output mapping are plotted in Fig. 4 (b), demonstrating nearly
 424 the same structure and mean values as in the previous case of constant inputs from
 425 the upstream layer. The coefficients in the case of Poisson inputs from the initial
 426 layer do display larger variance than in the constant stimulus vector case, but this
 427 is to be expected based on randomness introduced by the external spike train input.
 428 If instead of using the voltage jump $\gamma = 0.01$, a smaller jump size with higher mean
 429 input rate is used, such that the mean drive strength is fixed, the resultant drive

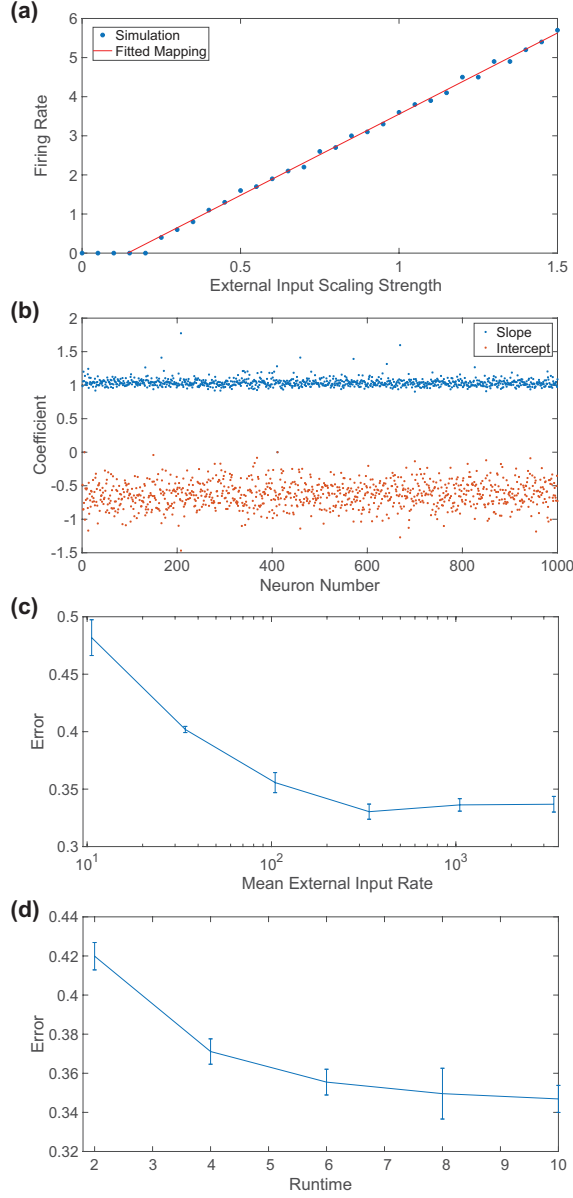


FIG. 4. (a) Gain curve for an individual downstream neuron in the two-layer network with current-based dynamics and Poisson spike train inputs from the initial layer, depicting the individual neuronal firing rate as a function of the external input strength across several simulations with ramped mean drive strengths. In each case, the voltage jump for the Poisson spike train is fixed at $\gamma = 0.01$ and the Poisson input rates are scaled. The input-output mapping for that individual neuron is fitted in the linear regime of the gain curve. (b) Slope and intercept coefficients in Eq. (3.3) fitted for each neuron in (a). (c) Relative reconstruction error dependence on the mean external spike train input rate. The external drive strength for the i^{th} downstream neuron is fixed at $(F_p)_i$ for $i = 1, \dots, m$ in each case. (d) Relative reconstruction error dependence on the time over which the dynamics described in (a) are recorded. In (c)-(d), the error is plotted over 5 realizations of the external input with error bars giving the standard deviation across realizations. CS reconstructions are obtained using the linear system given by Eq. (4.2) (c) and Fig. 2 (c) as input.

430 is statistically closer to the original constant input vector considered previously and
 431 tighter clustering of the coefficients is achieved.

432 As long as the rates of the Poisson spike train inputs are sufficiently high, such that
 433 each downstream neuron receives a relatively large number of upstream spikes over
 434 the observation time, the CS reconstructions obtained using the data-driven mapping
 435 display accuracy and stability properties analogous to those discussed for constant
 436 inputs. We illustrate this in Fig. 4 (c), where we hold the mean drive strength of the
 437 Poisson spike train inputs across the network constant while varying their mean rate
 438 and reconstructing the corresponding input stimulus given by Fig. 2 (c) in each case.
 439 For each choice of mean Poisson spike train rate, we fit the network input-output
 440 mapping over $0 \leq t \leq 10$ and observe little variability in the reconstruction error with
 441 accuracy comparable to the constant input case for sufficiently high mean input rates.
 442 For lower mean input rates, we note that longer observation times are necessary to
 443 well capture the stimulus structure and obtain an accurate reconstruction. As seen in
 444 Fig. 4 (d) for a successfully fitted network input-output mapping, the reconstruction
 445 error decreases initially with runtime before leveling off when enough downstream
 446 neuronal firing events are recorded to well encode the detailed stimulus features.

447 **5.2. Color Image Inputs.** To investigate if stimuli with color structure, more
 448 representative of natural scenes than gray-scale images, are well encoded along such
 449 compressive sensory pathways, we extend our model to RGB (red-green-blue) color
 450 image inputs. Here each stimulus in the input layer is represented by three constant
 451 n -vectors, corresponding to red, green, and blue intensities, respectively, across all
 452 n spatial locations of the pixels. We consider three networks of m downstream I&F
 453 neurons, each with unique feedforward and recurrent connectivity matrices, forced by
 454 the three respective color intensity vectors.

455 We fit the network input-output relationship using the downstream neuronal net-
 456 work responses to ramped constant artificial color image inputs with dynamics deter-
 457 mined by Eq. (2.1) across each of the three two-layer networks, producing three sets of
 458 coefficients for data-driven mapping (3.3). Then, we use the three sets of downstream
 459 neuronal firing rate measurements in response to a fixed color image stimulus to re-
 460 construct the corresponding intensity vectors across each of the three color channels
 461 via CS and Eq. (4.2). The three intensity vector reconstructions together yield the
 462 full color image input reconstruction. Note that since different photoreceptor types
 463 respond to different light wavelengths [70] and mammalian visual systems are known
 464 to often contain parallel channels [5], we choose to use three distinct compressive
 465 pathways to encode color images as opposed to a single pathway with fixed structure.

466 Several representative color image reconstructions are depicted in Fig. 5. Even
 467 in the case of color stimuli with realistic natural scene structure, we observe accurate
 468 reconstructions with errors computed across the three channels generally less than
 469 those observed in the case of 100×100 pixel gray-scale image inputs. Similar to
 470 the reconstructions of higher resolution gray-scale images, the larger number of total
 471 pixels across the three color channels facilitates more overall sparsity in the case of
 472 color images and thus improved CS reconstructions.

473 6. Reconstruction Framework for Alternative Network Models.

474 **6.1. Two-Layer Network Model with Conductance-Based Integrate-
 475 And-Fire Neuronal Dynamics.** While our initial analysis considered the dynamics
 476 of the downstream network when determined by current-based I&F neuronal activ-
 477 ity, we will now turn to more physiological neuronal models and later more realistic

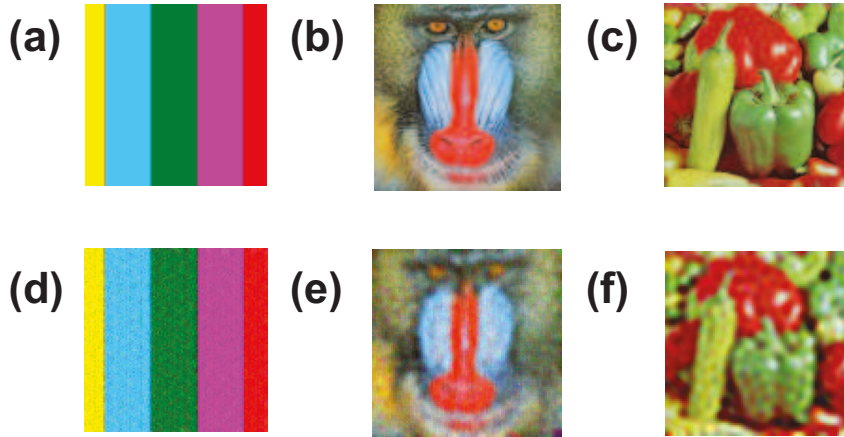


FIG. 5. (a)-(c): RGB color input image stimuli composed of 100×100 pixels for each of the three color intensity vectors (red, green, and blue). (d)-(f): Corresponding CS reconstructions of images in (a)-(c), respectively, using Eq. (4.2) and the network input-output mapping fitted for each color pathway. The relative reconstruction errors for (d)-(f) are 0.098, 0.134, and 0.1615, respectively. Each reconstruction uses a factor of 10 less downstream current-based I&F neurons than input pixels in each of the three two-layer networks corresponding to the three different color pathways.

478 network coupling. As a first step closer to biological realism, we instead assume that
 479 each downstream neuron is governed by conductance-based I&F dynamics. In the
 480 conductance-based model, synaptic input currents are now voltage-dependent and
 481 produce a richer repertoire of more biophysical dynamics [37, 79]. In particular, the
 482 membrane potential of the i^{th} downstream neuron now obeys

$$483 \quad (6.1) \quad \frac{dv_i}{dt} = -(v_i - V_R) - \left[\sum_{j=1}^n F_{ij} p_j + \frac{S}{N_R} \sum_{\substack{k=1 \\ k \neq i}}^m R_{ik} \sum_l \delta(t - \tau_{kl}) \right] (v_i - V_E),$$

484 where $V_E = 14/3$ is the excitatory reversal potential [77] and the remaining terms as
 485 well as the network structure are identical to the original two-layer model in Sect. 2.

486 We now apply our data-driven reconstruction approach to this alternative two-
 487 layer network model. First, we fit the input-output mapping (3.3) and then recon-
 488 struct constant gray-scale image inputs as outlined in Sect. 4. In Fig. 6 (a), we plot
 489 the firing rate of a single downstream neuron in response to ramped artificial con-
 490 stant inputs, similarly demonstrating linear gain for sufficiently strong input scaling
 491 strengths, and the resultant network input-output mapping is fit in the broad linear
 492 dynamical regime.

493 In Fig. 6 (b), we depict the corresponding slope and intercept coefficients in
 494 mapping (3.3) across the downstream layer. We observe coefficients distinct from
 495 those obtained previously, especially in the case of the slopes. Comparing Fig. 1 (b)
 496 and Fig. 6 (b), the two linear maps are fairly different, as the slopes and intercepts for
 497 the current-based model are clustered near 1 and -0.5 , respectively, while those for
 498 the conductance-based model are near 4.2 and -0.8 . This is to be expected because
 499 the analytically derived network input-output mapping in Eq. (3.1) does not apply to
 500 neurons with conductance-based dynamics governed by Eq. (6.1). Nevertheless, using

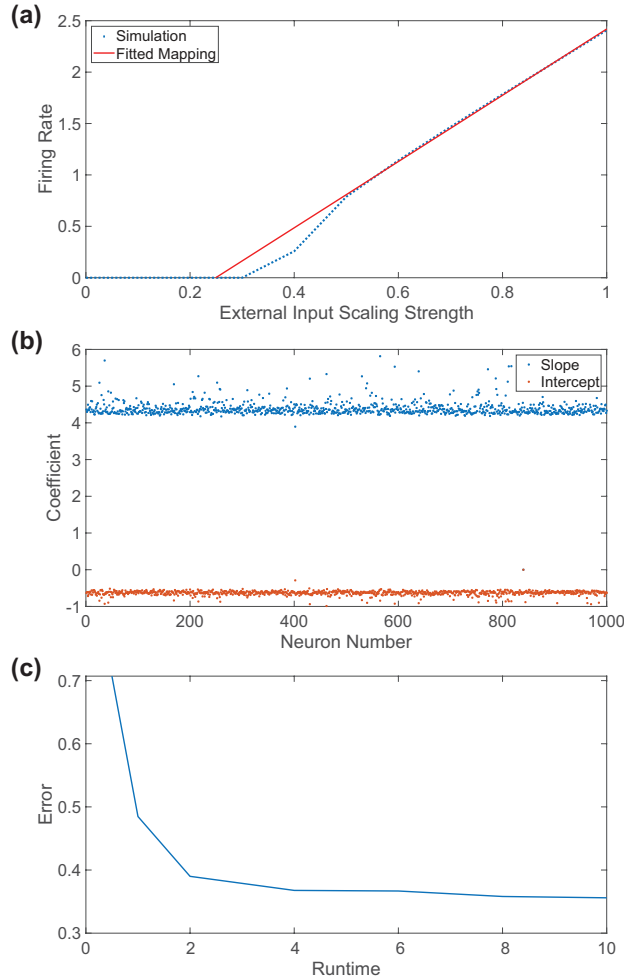


FIG. 6. (a) Gain curve for an individual downstream neuron in the two-layer network with conductance-based neuronal dynamics prescribed by Eq. (6.1), depicting the individual neuronal firing rate as a function of the external input scaling strength across several simulations with ramped constant external inputs. The input-output mapping for that individual neuron is fitted in the linear regime of the gain curve. (b) Slope and intercept coefficients in Eq. (3.3) fitted for each downstream neuron in the two-layer network considered in (a). (c) Relative reconstruction error as a function of the amount of time over which the network dynamics prescribed by Eq. (6.1) are recorded. Panel (c) considers the CS reconstruction of the image in Fig. 2 (c) utilizing a factor of 10 less downstream neurons than pixels and the linear system given by Eq. (4.2).

501 CS and the data-driven mapping, we recover input stimuli with accuracy comparable
 502 to the reconstructions obtained using the current-based neuronal network model. As
 503 shown in Fig. 6 (c), compressive encoding is indeed successful over relatively short
 504 time scales when the downstream neurons have conductance-based I&F dynamics.

505 **6.2. Two-Layer Network Model with Conductance-Based Integrate-
 506 And-Fire Neuronal Dynamics and Alpha-Function Coupling.** Beyond more
 507 detailed single neuron dynamics, we investigate the robustness of our compressive en-
 508 coding framework in the presence of more realistic recurrent neuronal communications

509 in the downstream layer. Reflecting the brief but finite time course of post-synaptic
 510 conductance changes induced by received action potentials, we replace the instantaneous
 511 Dirac delta function coupling between downstream neurons with a more phys-
 512 iological α -function time course for the neuronal interactions [101]. In this case, $\delta(t)$
 513 is replaced by

514 (6.2)
$$g(t) = \frac{t}{\sigma^2} \exp(-t/\sigma) H(t),$$

515 where $H(t)$ is the Heaviside function, such that $H(t) = 1$ for $t > 0$ and $H(t) = 0$
 516 otherwise, and the finite rise and decay time scales are both controlled by $\sigma = 1/20$
 517 (i.e., 1ms) [89, 76]. Aside from this change in coupling, we assume the individual
 518 downstream neuronal dynamics are conductance-based as in Eq. (6.1).

519 It is important to emphasize that in the case of this more realistic two-layer model
 520 network, analytically deriving an input-output mapping is intractable and thus our
 521 data-driven framework provides a more feasible alternative. We observe in Fig. 7
 522 (a) that the individual downstream neuronal firing rate response to sufficiently strong
 523 ramped constant external inputs is still linear; thus we apply our methodology to
 524 fit a data-driven network input-output mapping prescribed by Eq. (3.3) and obtain
 525 the corresponding coefficients plotted in Fig. 7 (b) across the downstream neuronal
 526 network. Though the data-driven mapping obtained is distinct from those gleaned
 527 for the prior models considered, we achieve similarly accurate input reconstructions
 528 for sufficiently long observation times, as displayed in Fig. 7 (c), highlighting the
 529 robustness of compressive encoding across sensory pathways with realistic neuronal
 530 dynamics. We expect that applying this reconstruction framework for alternative
 531 coupling models or different rise and decay time scales will produce comparable results
 532 once an appropriate data-driven network input-output mapping is obtained. For these
 533 alternative network models, it is also important to note that we are able to well fit
 534 the data-driven mapping with a very small number of ramped external inputs over a
 535 broad range of mean external input strengths as well as in the presence of noise, just
 536 as described for the current-based two-layer network model in Sect. 4.

537 **7. Spatially Localized Random Feedforward Connectivity.** In contrast
 538 with our previous investigations of encoding across compressive layers in light of in-
 539 creasing biological realism, which focused on the dynamics of individual downstream
 540 neurons, their communications, and their external input structure, we conclude by
 541 shifting our analysis to the impact of the feedforward connectivity organization.
 542 Receptive field structure in feedforward connectivity is shared throughout much of
 543 the visual, auditory, somatosensory, and olfactory systems in the sense that down-
 544 stream neurons are most stimulated by a range of stimuli with similar characteristics
 545 [60, 121, 118, 92, 75]. Across sensory system layers, one key consequence of receptive
 546 fields is spatial localization in stimulus sampling. In the retina, for example, gan-
 547 glion cells often exhibit center-surround receptive fields, such that the output of local
 548 clusters of photoreceptors is sampled by downstream ganglion cells, exciting ganglion
 549 cell activity in on-center locations and inhibiting activity in off-surround locations
 550 [120, 66].

551 To incorporate similar spatial structure into the two-layer network feedforward
 552 connectivity, each pixel in the n -component sampled image p is assigned a unique
 553 (x, y) location with integer coordinates on a $[1, \sqrt{n}] \times [1, \sqrt{n}]$ Cartesian grid reflecting
 554 all possible pixel locations. Each row of the feedforward connectivity matrix, F , is
 555 associated with a distinct random location (x_i, y_i) on this Cartesian grid, around

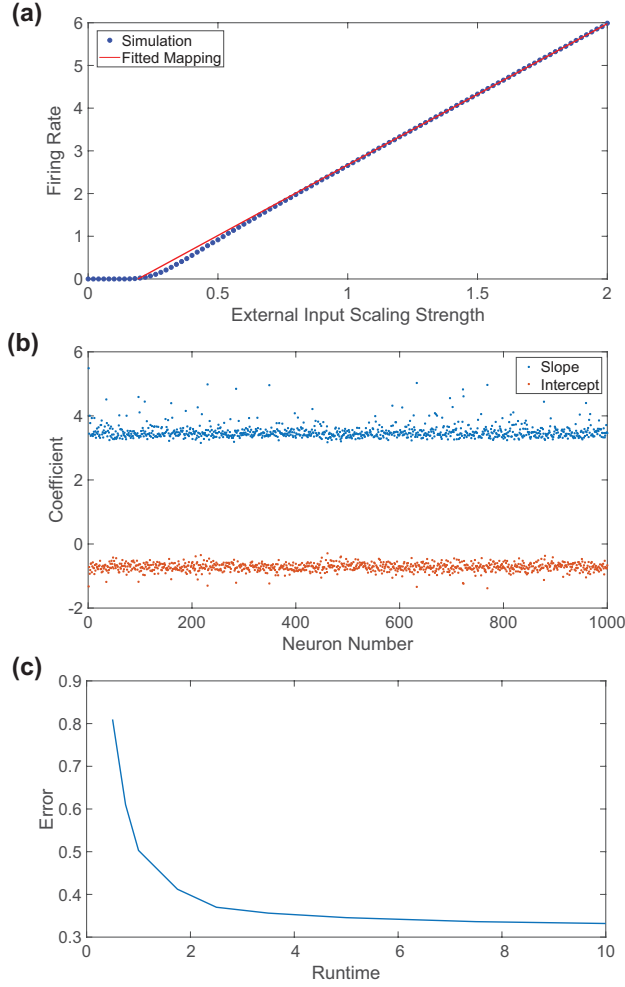


FIG. 7. (a) Gain curve for an individual downstream neuron in the two-layer network with conductance-based neuronal dynamics prescribed by Eq. (6.1) except with α -function coupling between downstream neurons given by Eq. (6.2), depicting the individual neuronal firing rate as a function of the external input scaling strength across several simulations with ramped constant external inputs. The input-output mapping for that individual neuron is fitted in the linear regime of the gain curve. (b) Slope and intercept coefficients in Eq. (3.3) fitted for each downstream neuron in the two-layer network considered in (a). (c) Relative reconstruction error as a function of the amount of time over which the network dynamics are recorded. Panel (c) considers the CS reconstruction of the image in Fig. 2 (c) utilizing a factor of 10 less downstream neurons than pixels and the linear system given by Eq. (4.2).

556 which the receptive field of the i^{th} downstream neuron is centered. Reflecting both
 557 spatial localization and some degree of randomness in the connectivity, we assume
 558 that the probability, P , that the i^{th} downstream neuron samples a pixel with spatial
 559 coordinates (x_j, y_j) is given by

560 (7.1)
$$P = \rho \exp(-[(x_i - x_j)^2 + (y_i - y_j)^2]/[2\sigma^2]),$$

561 where ρ is the sampling probability if $(x_i, y_i) = (x_j, y_j)$, that is when the receptive
 562 field center matches the location of a given pixel, and σ characterizes the distance

563 over which the receptive field samples pixels. Each feedforward connection in a given
 564 row i of F can therefore be described by a Bernoulli random variable, determined
 565 independently of all other entries of F , with success probability given by Eq. (7.1).

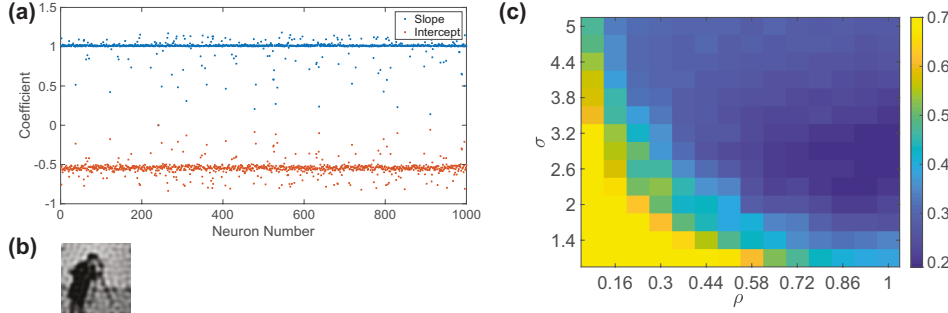


FIG. 8. (a) Slope and intercept coefficients in Eq. (3.3) fitted for each downstream neuron in the two-layer network with spatially localized random feedforward connectivity prescribed by Eq. (7.1). (b) CS reconstruction of the 100×100 pixel image in Fig. 2 (c) using the data-driven linear input-output mapping with coefficients in (a). The sampling probability parameter is $\rho = 0.9$, the sampling distance parameter is $\sigma = 2.5$, and the relative reconstruction error is 0.1933. (c) Relative reconstruction error dependence on the (ρ, σ) parameter choice. For each parameter choice, Fig. 2 (c) is reconstructed using a factor of 10 less downstream neurons than pixels and current-based neuronal dynamics prescribed by Eq. (2.1).

566 Previous work has demonstrated that, relative to the uniformly random feedfor-
 567 ward connectivity assumed earlier in this work, sampling analogous to this *spatially*
 568 *localized random feedforward connectivity* more accurately captures the dominant low
 569 and moderate frequency components composing an image when using a small number
 570 of linear samples [19, 21]. By applying our data-driven reconstruction framework,
 571 we examine if this more realistic feedforward connectivity structure is capable of well
 572 transmitting stimulus information across the type of compressive pathway modeled
 573 initially through the two-layer current-based I&F network discussed in Sect. 2. Even
 574 though the feedforward connectivity is now distinct from the uniformly random struc-
 575 ture discussed earlier, the slope and intercept coefficients of the resultant network
 576 input-output mapping, plotted in Fig. 8 (a), have nearly the same mean values as
 577 found previously for downstream neurons with current-based I&F dynamics. Compar-
 578 ing with Fig. 1 (b), relatively uniform clustering about the means is observed in each
 579 case, though the variance of the coefficients in the spatially localized case is smaller.
 580 This suggests that the network input-output mapping structure is largely determined
 581 by the dynamics of the individual downstream neurons and the time course of their
 582 communications, which were both shown to impact the fitted coefficients in Sect. 6,
 583 whereas the feedforward connectivity structure plays more of a role in determining the
 584 stimulus features that are well captured by the downstream network dynamics. The
 585 optimal CS reconstruction obtained using spatially localized random feedforward con-
 586 nectivity and the data-driven network input-output mapping for the input stimulus in
 587 Fig. 2 (c) is displayed in Fig. 8 (b), exhibiting a reconstruction error approximately
 588 half that obtained originally using uniformly random feedforward connectivity.

589 Since the success of the stimulus encoding in the downstream neuronal dynamics
 590 may be intimately tied to the receptive field size and density, we vary feedforward
 591 connectivity parameters, ρ and σ , and plot the reconstruction error for each parameter
 592 choice in Fig. 8 (c). The optimal σ generates moderately-sized receptive fields and the

593 corresponding optimal choice of ρ is sufficiently large such that each pixel is expected
 594 to be sampled at least once. A local minimum in reconstruction error occurs near
 595 $\sigma \approx 2.5$, and even when ρ is as high as $\rho \approx 0.9$, which corresponds to the reconstruction
 596 in Fig. 8 (b), the feedforward connectivity matrix is sparse with a connection density
 597 of only approximately 0.001. Increasing ρ yet further for fixed σ has little impact
 598 on reconstruction quality in this case, and 1 is the upper bound for ρ based on its
 599 probabilistic interpretation.

600 We remark that for simultaneously large ρ and σ , each receptive field collects
 601 information from too much of the visual field, resulting in redundancy in the im-
 602 age information obtained by each downstream neuron akin to the uniformly random
 603 connectivity considered originally. In this case, a high correlation in the input data re-
 604 ceived across the downstream network results in diminished reconstruction accuracy.
 605 Likewise, for simultaneously small ρ and σ , each receptive field may gather insuffi-
 606 cient information across pixel locations and the input into the downstream neurons
 607 may be too small to drive the firing events necessary to encode stimulus information,
 608 generating extremely large reconstruction error. Overall, for moderately sized recep-
 609 tive fields with relatively sparse connectivity, as often observed in vivo, improved CS
 610 reconstructions are achieved. This gives further credence to the hypothesis that sen-
 611 sory systems have evolved to exhibit structure optimized for efficient natural stimulus
 612 encoding across compressive pathways.

613 **8. Discussion and Conclusions.** We have developed a potential mechanism
 614 for the preservation of stimulus information across the ubiquitous compressive path-
 615 ways in the brain, demonstrating its suitability in the context of numerous two-layer
 616 network models with varying degrees of biological realism in both the dynamics of
 617 individual neurons and their coupling. Our novel framework for reconstructing input
 618 layer information from the nonlinear neuronal activity of a compressive downstream
 619 layer was completely driven by simulation data and did not require knowledge of the
 620 dynamical system governing the model activity. We approximated a network input-
 621 output mapping based on the linear firing rate response of the downstream neurons to
 622 a small number of ramped artificial inputs, which is a feature shared by all models in-
 623 vestigated in this work for sufficiently strong external input strengths. In conjunction
 624 with compressive sensing reconstruction techniques, we used this data-driven net-
 625 work input-output relationship to reconstruct realistic input stimuli taking the form
 626 of gray-scale natural scenes, color images, and image-driven Poisson spike trains. By
 627 incorporating characteristics of spatial receptive fields into the feedforward connectiv-
 628 ity, we also showed that the encoding properties of the downstream neuronal network
 629 dynamics are in fact improved, as expected by the prevalence of receptive fields across
 630 sensory systems.

631 This work provides a new proof of concept supporting the notion that such com-
 632 pressive pathways, if designed intelligently, well preserve stimulus information with
 633 great efficiency. By containing significantly less neurons in the first downstream layer,
 634 stimuli may be rapidly processed in ways that improve encoding capability in the
 635 subsequent expansive downstream layers with minimal energy expenditure required
 636 [67, 115, 104, 98, 13, 23, 48]. Such processing in the compressive layer may help
 637 to reduce redundancy and enhance the function of sensory pathways in performing
 638 commonly encountered tasks, such as classification [71, 41].

639 While our two-layer model was meant to capture the primary shared features
 640 of compressive pathways and their mechanisms for stimulus encoding, it would be
 641 informative to extend our analysis to models with more detailed physiological struc-

ture corresponding to a specific early sensory system pathway. Such an investigation would benefit from incorporating yet more detailed neuronal activity. We emphasize that even in these more realistic model settings, the linear gain in neuronal response leveraged in our analysis is commonly observed [30, 54, 15, 117], and thus we expect our framework to be naturally extended to such models where analytical techniques, such as coarse-graining, become intractable. Even for highly nonlinear single neuron models, such as the Hodgkin-Huxley model, previous work has successfully produced approximately linear gain curves in the presence of various additional realistic ion channels with dynamics over a range of time scales [74, 25], and the presence of negative feedback in the form of biophysical adaptation currents is known to linearize gain curves that are nonlinear when unadapted [51].

Though our analysis focused on the activity of a downstream layer of excitatory neurons that were largely mean-driven, networks containing additional inhibitory neurons in alternative dynamical regimes, such as the balanced operating state [14, 116, 113], also demonstrate a highly sensitive and linear increase in neuronal activity with external input strength. In general, the neuronal gain curve has been shown to adapt to different stimulus conditions, such as light level in the context of the visual system [27], and potential improvements in stimulus encoding along compressive pathways leveraging this adaptation would mark an interesting area of future investigation. Since our methodology specifically considers dynamical regimes exhibiting linear firing rate gain, it is worth noting that the single neuron models we had analyzed and neurons in experiment nonetheless demonstrate nonlinear voltage dynamics, which are important in their own right and have been shown to enhance feature selectivity [58] as well as decorrelate neuronal responses to stimuli [95, 73].

By more closely mimicking the structure of compressive feedforward pathways, yet further improvements in encoding may be possible using our reconstruction methodology. The size of receptive fields varies widely within a sensory pathway and depending on the receptive field size, details of various scales are measured [99, 45], akin to adjusting the σ parameter in our model of feedforward connectivity with spatially localized structure. By incorporating a diversity of receptive field sizes, we hypothesize that lower amplitude frequency component contributions may be successfully captured with the same number of downstream neurons. Including center-surround antagonism in the feedforward connectivity, which could be modeled using a difference of Gaussians [122, 50], may facilitate the encoding of finer edge information in the downstream neuronal dynamics. Reflecting the architecture of the primary visual cortex by including simple cells in further downstream layers [65, 93], modeled via Gabor functions [42, 85, 72], could also result in orientation selectivity. It would be natural to investigate if additional receptive field types as well as multiple compressive and expansive layers would further improve the encoding of higher order stimulus features. Including these physiological details in the engineering of prosthetic sensory devices and adapting our reconstruction framework to send realistic signals across artificial compressive pathways presents a potential approach to better mitigating sensory impairments [78, 24].

Since *in vivo* neuronal recordings have been shown to exhibit a linear increase in response with scaled external inputs in certain dynamical regimes [117, 96, 81, 61], our developed framework is likely generalizable to experimental settings seeking to approximate neuronal input-output mappings by making use of intracellular and multielectrode array recordings in response to ramped optogenetic forcing [97, 94]. Once the network input-output relationship is obtained across a pathway of interest, similar CS techniques may be leveraged in order to recover sparse and large-scale neuronal

692 network connectivity [20, 106, 125, 12]. Since directly measuring structural neuronal
 693 connectivity is infeasible for large networks due to, for example, limitations on the
 694 spatial resolution of measurement technology [107, 59, 53], such efficient connectivity
 695 reconstructions based on recordings of neuronal dynamics are especially valuable in
 696 characterizing the structure-function relationship of networks in the brain.

697

698 **Appendix A. Derivation of the Theoretical Input-Output Mapping for
 699 the Current-Based Integrate-And-Fire Neuronal Network.**

700

701 In deriving the theoretical input-output mapping given by Eq. (3.1), we leverage
 702 a coarse-graining approach that applies probabilistic arguments to ultimately obtain
 703 a static, linear system relating the network input, stimulus vector p , to the network
 704 output, namely the vector of individual downstream neuronal firing rates μ . We
 705 focus our analysis in this Appendix on the two-layer current-based integrate-and-fire
 706 neuronal network given by Eq. (2.1) because it is analytically tractable, and since
 707 this argument does not well extend to more detailed modeling frameworks, we instead
 708 resort to our newly developed data-driven approach in the remainder of this work.

709 We start by analyzing a statistical ensemble of almost identical networks that
 710 differ only in their initial membrane potentials, $v_i(t = 0)$, and their resultant input
 711 currents, for $i = 1, \dots, m$. For each realization of the network, the i^{th} downstream
 712 neuron is hence driven by a new independent spike train transmitted by its pre-
 713 connected neighbors as well as the external input current, $\sum_{j=1}^n F_{ij} p_j$. For each
 714 realization of the network in the ensemble, the feed-forward and recurrent connectivity
 715 matrices, F and R , respectively, remain fixed.

716 To more tractably characterize the total drive into each downstream neuron, we
 717 assume the network exhibits a large number of firing events, of which each only evokes
 718 a relatively small voltage jump to post-connected neurons as typical in vivo. This
 719 implies high spike frequency, $\mu_i \gg 0$, and small spike magnitude, $S/N_R \approx 0$. The
 720 total recurrent network input into each downstream neuron, say the i^{th} , is

$$721 \quad \frac{S}{N_R} \sum_{\substack{k=1 \\ k \neq i}}^m R_{ik} \sum_l \delta(t - \tau_{kl}),$$

722 and therefore may be approximated by a Poisson spike train [39]. Statistically, the
 723 effect of the rapid recurrent network input approaches the mean drive from pre-
 724 connected neurons,

$$725 \quad (\text{A.1}) \quad \frac{S}{N_R} \sum_{\substack{k=1 \\ k \neq i}}^m R_{ik} \mu_k.$$

726 Replacing the rightmost term of Eq. (2.1) by Eq. (A.1), we obtain the voltage at
 727 time t for the i^{th} downstream neuron

$$728 \quad v_i(t) = v_i(t_0) e^{-(t-t_0)} + \left(1 - e^{-(t-t_0)}\right) \\ 729 \quad (\text{A.2}) \quad \times \left(V_R + \sum_{j=1}^n F_{ij} p_j + \frac{S}{N_R} \sum_{\substack{k=1 \\ k \neq i}}^m R_{ik} \mu_k \right).$$

730

731 Letting $v_i(t_0) = V_R$, the resting voltage, implies a firing event is expected to occur
 732 when $v_i(t_0 + 1/\mu_i) = V_T$, where μ_i is the firing rate of the i^{th} downstream neuron.
 733 To obtain a static, nonlinear input-output mapping, we divide by $1 - e^{-1/\mu_i}$, yielding

734 (A.3)
$$\sum_{j=1}^n F_{ij} p_j = \frac{V_T - V_R}{1 - e^{-1/\mu_i}} - \frac{S}{N_R} \sum_{\substack{k=1 \\ k \neq i}}^m R_{ik} \mu_k.$$

735 To linearize this mapping, we leverage the earlier assumption that the downstream
 736 network is in a high-firing-rate dynamical regime. We Taylor expand with respect to
 737 the small parameter $1/(\mu_i)$ and up to the leading order $O(1/(\mu_i)^2)$, we obtain

738 (A.4)
$$\sum_{j=1}^n F_{ij} p_j = \mu_i (V_T - V_R) + \frac{(V_T - V_R)}{2} - \frac{S}{N_R} \sum_{\substack{k=1 \\ k \neq i}}^m R_{ik} \mu_k.$$

739 Rewriting Eq. (A.4) across the downstream network, for $i = 1, \dots, m$, yields the
 740 static, linear input-output mapping equivalent to Eq. (3.1),

741 (A.5)
$$Fp = \left(\mu + \frac{e_m}{2} \right) (V_T - V_R) - \frac{S}{N_R} R \mu,$$

742 where e_m denotes an m -vector of ones. To more closely compare with the data-driven
 743 mapping given by Eq. (3.3), we isolate μ above and obtain

744 (A.6)
$$\left(I - \frac{S}{N_R (V_T - V_R)} R \right) \mu = \frac{Fp}{(V_T - V_R)} - \frac{e_m}{2}.$$

745 Expanding in the form of a Neumann series yields

746 (A.7)
$$\mu \approx \left(I + \frac{S}{N_R (V_T - V_R)} R + \dots \right) \left(\frac{Fp}{(V_T - V_R)} - \frac{e_m}{2} \right).$$

747 To leading order, we observe that Eq. (A.7) takes a form analogous to the data-driven
 748 mapping, where comparing the mappings shows that across the downstream network
 749 the fitted coefficients in this case are $\alpha \approx \frac{1}{(V_T - V_R)}$ and $\beta \approx -\frac{1}{2}$. We also see that the
 750 correction term in Eq. (A.7) implies that μ is generally modulated by the number
 751 of incoming recurrent connections. This is a primary motivation for the inclusion of
 752 the N_R term that normalizes the recurrent connectivity matrix by the total number
 753 of recurrent connections in the two-layer network model framework, which keeps the
 754 total drive across the downstream network approximately constant with changes in
 755 the connection density of R .

756 REFERENCES

757 [1] L. ABBOTT, *Lapicque's introduction of the integrate-and-fire model neuron (1907)*, Brain
 758 research bulletin, 50 (1999), pp. 303–304.
 759 [2] K. AMANO, N. GODA, S. NISHIDA, Y. EJIMA, T. TAKEDA, AND Y. OHTANI, *Estimation of the*
 760 *timing of human visual perception from magnetoencephalography*, J. Neurosci., 26 (2006),
 761 pp. 3981–3991.
 762 [3] S. ANDO, Y. YAMADA, AND M. KOKUBU, *Reaction time to peripheral visual stimuli during*
 763 *exercise under hypoxia*, J. Appl. Physiol., 108 (2010), pp. 1210–1216.
 764 [4] B. BABADI AND H. SOMPOLINSKY, *Sparseness and expansion in sensory representations*, Neu-
 765 *ron*, 83 (2014), pp. 1213–1226.

766 [5] T. BADEN, P. BERENS, K. FRANKE, M. ROMAN ROSON, M. BETHGE, AND T. EULER, *The*
 767 *functional diversity of retinal ganglion cells in the mouse*, *Nature*, 529 (2016), pp. 345–
 768 350.

769 [6] W. BAIR, C. KOCH, W. NEWSOME, AND K. BRITTON, *Power spectrum analysis of bursting*
 770 *cells in area MT in the behaving monkey*, *J. Neurosci.*, 14 (1994), pp. 2870–2892.

771 [7] R. BARANIUK, *Compressive sensing*, *IEEE Signal Processing Mag.*, (2007), pp. 118–120.

772 [8] H. BARLOW, *Redundancy reduction revisited.*, *Network*, 12 (2001), pp. 241–253.

773 [9] H. B. BARLOW, *The coding of sensory messages*, in *Current Problems in Animal Behaviour*,
 774 W. H. Thorpe and O. L. Zangwill, eds., Cambridge University Press, 1961, pp. 331–360.

775 [10] H. B. BARLOW, *The ferrier lecture, 1980. critical limiting factors in the design of the eye*
 776 *and visual cortex*, *Proc R Soc Lond B Biol Sci*, 212 (1981), pp. 1–34.

777 [11] V. BARRANCA, G. KOVACIC, AND D. ZHOU, *The role of sparsity in inverse problems for*
 778 *networks with nonlinear dynamics*, (2019), pp. 1291–1311, <https://doi.org/10.4310/CMS.2019.v17.n5.a6>.

780 [12] V. BARRANCA, D. ZHOU, AND D. CAI, *Compressive sensing reconstruction of feed-forward*
 781 *connectivity in pulse-coupled nonlinear networks*, *Phys. Rev. E*, 93 (2016), p. 060201,
 782 <https://doi.org/10.1103/PhysRevE.93.060201>.

783 [13] V. J. BARRANCA, H. HUANG, AND G. KAWAKITA, *Network structure and input integration in*
 784 *competing firing rate models for decision-making*, *J Comput Neurosci*, 46 (2019), pp. 145–
 785 168.

786 [14] V. J. BARRANCA, H. HUANG, AND S. LI, *The impact of spike-frequency adaptation on balanced*
 787 *network dynamics*, *Cogn Neurodyn*, 13 (2019), pp. 105–120.

788 [15] V. J. BARRANCA, D. C. JOHNSON, J. L. MOYHER, J. P. SAUPPE, M. S. SHKARAYEV,
 789 G. KOVACIC, AND D. CAI, *Dynamics of the exponential integrate-and-fire model with*
 790 *slow currents and adaptation*, *J. Comput. Neurosci.*, 37 (2014), pp. 161–180.

791 [16] V. J. BARRANCA, G. KOVACIC, D. ZHOU, AND D. CAI, *Network dynamics for optimal*
 792 *compressive-sensing input-signal recovery*, *Phys. Rev. E*, 90 (2014), p. 042908.

793 [17] V. J. BARRANCA, G. KOVACIC, D. ZHOU, AND D. CAI, *Sparsity and compressed coding in*
 794 *sensory systems*, *PLoS Comput. Biol.*, 10 (2014), p. e1003793.

795 [18] V. J. BARRANCA, G. KOVACIC, D. ZHOU, AND D. CAI, *Efficient image processing via com-*
 796 *pressive sensing of integrate-and-fire neuronal network dynamics*, *Neurocomputing*, 171
 797 (2016), pp. 1313 – 1322, <https://doi.org/http://dx.doi.org/10.1016/j.neucom.2015.07.067>, <http://www.sciencedirect.com/science/article/pii/S092523215010747>.

798 [19] V. J. BARRANCA, G. KOVACIC, D. ZHOU, AND D. CAI, *Improved Compressive Sensing of*
 799 *Natural Scenes Using Localized Random Sampling*, *Sci. Rep.*, 6 (2016), p. 31976.

800 [20] V. J. BARRANCA AND D. ZHOU, *Compressive Sensing Inference of Neuronal Network Con-*
 801 *nectivity in Balanced Neuronal Dynamics*, *Front. Neurosci.*, 13 (2019), p. 1101.

802 [21] V. J. BARRANCA AND X. G. ZHU, *A computational study of the role of spatial receptive*
 803 *field structure in processing natural and non-natural scenes*, *J. Theor. Biol.*, 454 (2018),
 804 pp. 268–277.

805 [22] A. BLUM, *Random projection, margins, kernels, and feature-selection*, in *Proceedings of*
 806 *the 2005 International Conference on Subspace, Latent Structure and Feature Selection*,
 807 *SLSFS'05*, Berlin, Heidelberg, 2005, Springer-Verlag, p. 52–68.

808 [23] R. BOGACZ, M. USHER, J. ZHANG, AND J. L. McCLELLAND, *Extending a biologically in-*
 809 *spired model of choice: multi-alternatives, nonlinearity and value-based multidimensional*
 810 *choice*, *Philos. Trans. R. Soc. Lond. B, Biol. Sci.*, 362 (2007), pp. 1655–1670.

811 [24] P. BONIFAZI, F. DIFATO, P. MASSOBROIO, G. L. BRESCHI, V. PASQUALE, T. LEVI, M. GOLDIN,
 812 Y. BORNAT, M. TEDESCO, M. BISIO, S. KANNER, R. GALRON, J. TESSADORI, S. TAVERNA,
 813 AND M. CHIAPPALONE, *In vitro large-scale experimental and theoretical studies for the*
 814 *realization of bi-directional brain-prostheses*, *Front. Neural Circuits*, 7 (2013), p. 40.

815 [25] A. BORISYUK AND J. RINZEL, *Understanding neuronal dynamics by geometrical dissection of*
 816 *minimal models*, *Methods and Models in Neurophysics* (1st Ed., Elsevier, 2005), (2005),
 817 pp. 17–72.

818 [26] M. BRECHT AND B. SAKMANN, *Dynamic representation of whisker deflection by synaptic*
 819 *potentials in spiny stellate and pyramidal cells in the barrels and septa of layer 4 rat*
 820 *somatosensory cortex*, *J. Physiol.*, 543 (2002), pp. 49–70.

821 [27] N. BRENNER, W. BIALEK, AND R. DE RUYTER VAN STEVENINCK, *Adaptive rescaling maximizes*
 822 *information transmission*, *Neuron*, 26 (2000), pp. 695–702.

823 [28] R. BRETT, M. RUDOLPH, T. CARNEVALE, M. HINES, D. BEEMAN, J. M. BOWER, M. DIES-
 824 MANN, A. MORRISON, P. H. GOODMAN, F. C. HARRIS JR, M. ZIRPE, T. NATSCHLAGER,
 825 D. PECEVSKI, B. ERMENTROUT, M. DJURFELDT, A. LANSNER, O. ROCHEL, T. VIEVILLE,
 826 E. MULLER, A. P. DAVISON, S. E. BOUSTANI, AND A. DESTEXHE, *Simulation of networks*

of spiking neurons: A review of tools and strategies, *J. Comput. Neurosci.*, 23 (2007), pp. 349–398.

[29] A. BRUCKSTEIN, D. DONOHO, AND M. ELAD, *From sparse solutions of systems of equations to sparse modeling of signals and images*, SIAM Review, 51 (2009), pp. 34–81.

[30] N. BRUNEL AND P. LATHAM, *Firing rate of the noisy quadratic integrate-and-fire neuron*, *Neural Comp.*, 15 (2003), pp. 2281–2306.

[31] A. BURKITT, *A review of the integrate-and-fire neuron model: I. homogeneous synaptic input*, *Biol. Cybern.*, 95 (2006), pp. 1–19, <https://doi.org/10.1007/s00422-006-0068-6>.

[32] D. CAI, A. RANGAN, AND D. McLAUGHLIN, *Architectural and synaptic mechanisms underlying coherent spontaneous activity in V1*, *Proc. Nat'l Acad. Sci (USA)*, 102 (2005), pp. 5868–5873.

[33] D. CAI, L. TAO, A. V. RANGAN, AND D. W. McLAUGHLIN, *Kinetic theory for neuronal network dynamics*, *Commun. Math. Sci.*, 4 (2006), pp. 97–127.

[34] D. CAI, L. TAO, M. SHELLEY, AND D. McLAUGHLIN, *An effective representation of fluctuation-driven neuronal networks with application to simple & complex cells in visual cortex*, *Proc. Nat. Acad. Sci.*, 101 (2004), pp. 7757–7762.

[35] E. CANDES, J. ROMBERG, AND T. TAO, *Stable signal recovery from incomplete and inaccurate measurements*, *Commun. Pur. Appl. Math.*, 59 (2006), pp. 1207–1223.

[36] E. J. CANDES AND M. B. WAKIN, *An Introduction To Compressive Sampling*, *Signal Process. Mag.*, IEEE, 25 (2008), pp. 21–30.

[37] S. CAVALLARI, S. PANZERI, AND A. MAZZONI, *Comparison of the dynamics of neural interactions between current-based and conductance-based integrate-and-fire recurrent networks*, *Front. Neural. Circuits*, 8 (2014), p. 12.

[38] G. B. CHOI, D. D. STETTLER, B. R. KALLMAN, S. T. BHASKAR, A. FLEISCHMANN, AND R. AXEL, *Driving opposing behaviors with ensembles of piriform neurons*, *Cell*, 146 (2011), pp. 1004–1015.

[39] E. CINLAR, *Superposition of point processes*, in *Stochastic Point Processes: Statistical Analysis, Theory, and Applications*, P. Lewis, ed., Wiley, New York, NY, 1972, pp. 549–606.

[40] W. K. COULTER, C. J. HILLAR, G. ISLEY, AND F. T. SOMMER, *Adaptive compressed sensing - a new class of self-organizing coding models for neuroscience*, in *ICASSP, IEEE*, 2010, pp. 5494–5497.

[41] S. DASGUPTA, C. F. STEVENS, AND S. NAVLAKHA, *A neural algorithm for a fundamental computing problem*, *Science*, 358 (2017), pp. 793–796.

[42] J. G. DAUGMAN, *Two-dimensional spectral analysis of cortical receptive field profiles*, *Vision Res.*, 20 (1980), pp. 847–856.

[43] P. DAYAN AND L. ABBOTT, *Theoretical Neuroscience*, MIT press, Cambridge, MA, 2001.

[44] D. J. DEBOER AND D. I. VANHEY, *Gap-junction communication between subtypes of direction-selective ganglion cells in the developing retina*, *J. Comp. Neurol.*, 482 (2005), pp. 85–93.

[45] R. DESIMONE, T. D. ALBRIGHT, C. G. GROSS, AND C. BRUCE, *Stimulus-selective properties of inferior temporal neurons in the macaque*, *J. Neurosci.*, 4 (1984), pp. 2051–2062.

[46] D. DONOHO, *Compressed sensing*, *IEEE Trans. Inform. Theory*, 52 (2006), pp. 1289–1306.

[47] D. DONOHO AND Y. TSAIG, *Fast solution of l_1 -norm minimization problems when the solution may be sparse*, *IEEE Trans. Inform. Theory*, 54 (2008), pp. 4789–4812.

[48] R. J. DOUGLAS AND K. A. MARTIN, *Recurrent neuronal circuits in the neocortex*, *Curr. Biol.*, 17 (2007), pp. 496–500.

[49] F. A. DUNN AND F. RIEKE, *The impact of photoreceptor noise on retinal gain controls*, *Curr. Opin. Neurobiol.*, 16 (2006), pp. 363–370.

[50] J. H. ELDER AND A. J. SACHS, *Psychophysical receptive fields of edge detection mechanisms*, *Vision Res.*, 44 (2004), pp. 795–813.

[51] B. ERMENTROUT, *Linearization of f_i curves by adaptation*, *Neural computation*, 10 (1998), pp. 1721–1729.

[52] D. FIELD, *What is the goal of sensory coding?*, *Neural Computation*, 6 (1994), pp. 559–601, <https://doi.org/10.1162/neco.1994.6.4.559>.

[53] G. D. FIELD, J. L. GAUTHIER, A. SHER, M. GRESCHNER, T. A. MACHADO, L. H. JEPSON, J. SHLENS, D. E. GUNNING, K. MATHIESON, W. DABROWSKI, L. PANINSKI, A. M. LITKE, AND E. J. CHICHILNISKY, *Functional connectivity in the retina at the resolution of photoreceptors*, *Nature*, 467 (2010), pp. 673–677.

[54] N. FOURCAUD-TROCMÉ AND N. BRUNEL, *Dynamics of the instantaneous firing rate in response to changes in input statistics*, *J Comput Neurosci*, 18 (2005), pp. 311–321.

[55] S. GANGULI AND H. SOMPOLINSKY, *Short-term memory in neuronal networks through dynamical compressed sensing*, in *NIPS*, Curran Associates, Inc., 2010, pp. 667–675.

[56] S. GANGULI AND H. SOMPOLINSKY, *Compressed sensing, sparsity, and dimensionality in neu-*

ronal information processing and data analysis, *Annu. Rev. Neurosci.*, 35 (2012), pp. 485–508.

[57] E. GAMMOR, R. SEGEV, AND E. SCHNEIDMAN, *The architecture of functional interaction networks in the retina*, *J. Neurosci.*, 31 (2011), pp. 3044–3054.

[58] T. GOLLISCH, *Features and functions of nonlinear spatial integration by retinal ganglion cells*, *J. Physiol. Paris*, 107 (2013), pp. 338–348.

[59] M. GOMEZ-RODRIGUEZ, J. LESKOVEC, AND A. KRAUSE, *Inferring networks of diffusion and influence*, *T. Knowl. Discov. D.*, 5 (2012), p. 21, <https://doi.org/10.1145/2086737.2086741>.

[60] M. S. GRAZIANO AND C. G. GROSS, *A bimodal map of space: somatosensory receptive fields in the macaque putamen with corresponding visual receptive fields*, *Exp Brain Res*, 97 (1993), pp. 96–109.

[61] W. N. GRIMES, G. W. SCHWARTZ, AND F. RIEKE, *The synaptic and circuit mechanisms underlying a change in spatial encoding in the retina*, *Neuron*, 82 (2014), pp. 460–473.

[62] Y. HE, Z. J. CHEN, AND A. C. EVANS, *Small-world anatomical networks in the human brain revealed by cortical thickness from MRI*, *Cereb. Cortex*, 17 (2007), pp. 2407–2419.

[63] C. HEIL AND D. WALNUT, *Continuous and discrete wavelet transforms*, *SIAM review*, 31 (1989), pp. 628–666.

[64] T. HROMADKA, M. R. DEWEES, AND A. M. ZADOR, *Sparse representation of sounds in the unanesthetized auditory cortex*, *PLoS Biol.*, 6 (2008), p. e16.

[65] D. H. HUBEL AND T. N. WIESEL, *Receptive fields of single neurones in the cat's striate cortex*, *J Physiol*, 148 (1959), pp. 574–591.

[66] D. H. HUBEL AND T. N. WIESEL, *Receptive fields of optic nerve fibres in the spider monkey*, *J Physiol*, 154 (1960), pp. 572–580.

[67] M. HUMPHRIES, K. GURNEY, AND T. PRESCOTT, *The brainstem reticular formation is a small-world, not scale-free, network*, *Proc. Biol. Sci.*, 273 (2006), pp. 503–511, <https://doi.org/10.1098/rspb.2005.3354>.

[68] G. ISLEY, C. J. HILLAR, AND F. T. SOMMER, *Deciphering subsampled data: adaptive compressive sampling as a principle of brain communication*, in *NIPS*, Curran Associates, Inc., 2010, pp. 910–918.

[69] E. M. IZHKEVICH, *Which model to use for cortical spiking neurons?*, *IEEE Trans. Neural Netw.*, 15 (2004), pp. 1063–1070.

[70] G. H. JACOBS, *Primate photopigments and primate color vision*, *Proc. Natl. Acad. Sci. USA*, 93 (1996), pp. 577–581.

[71] J. M. JEANNE AND R. I. WILSON, *Convergence, Divergence, and Reconvergence in a Feedforward Network Improves Neural Speed and Accuracy*, *Neuron*, 88 (2015), pp. 1014–1026.

[72] J. P. JONES AND L. A. PALMER, *An evaluation of the two-dimensional Gabor filter model of simple receptive fields in cat striate cortex*, *J. Neurophysiol.*, 58 (1987), pp. 1233–1258.

[73] D. B. KASTNER, S. A. BACCUS, AND T. O. SHARPEE, *Critical and maximally informative encoding between neural populations in the retina*, *Proc. Natl. Acad. Sci. USA*, 112 (2015), pp. 2533–2538.

[74] T. J. KISPERSKY, J. S. CAPLAN, AND E. MARDER, *Increase in sodium conductance decreases firing rate and gain in model neurons*, *Journal of Neuroscience*, 32 (2012), pp. 10995–11004.

[75] E. I. KNUDSEN AND M. KONISHI, *Center-surround organization of auditory receptive fields in the owl*, *Science*, 202 (1978), pp. 778–780.

[76] C. KOCH, *Biophysics of Computation*, Oxford University Press, Oxford, 1999.

[77] G. KOVÁČIČ, L. TAO, A. V. RANGAN, AND D. CAI, *Fokker-planck description of conductance-based integrate-and-fire neuronal networks*, *Phys. Rev. E*, 80 (2009), p. 021904.

[78] K. KRUG, C. D. SALZMAN, AND S. WADDELL, *Understanding the brain by controlling neural activity*, *Philos. Trans. R. Soc. Lond. B Biol. Sci.*, 370 (2015), p. 20140201.

[79] A. KUHN, A. AERTSEN, AND S. ROTTER, *Neuronal integration of synaptic input in the fluctuation-driven regime*, *J. Neurosci.*, 24 (2004), pp. 2345–2356.

[80] R. J. KULESZA, A. VINUELA, E. SALDANA, AND A. S. BERREBI, *Unbiased stereological estimates of neuron number in subcortical auditory nuclei of the rat*, *Hear. Res.*, 168 (2002), pp. 12–24.

[81] G. LA CAMERA, A. RAUCH, D. THURBON, H. R. LUSCHER, W. SENN, AND S. FUSI, *Multiple time scales of temporal response in pyramidal and fast spiking cortical neurons*, *J. Neurophysiol.*, 96 (2006), pp. 3448–3464.

[82] Y. LECUN, Y. BENGIO, AND G. HINTON, *Deep learning*, *Nature*, 521 (2015), pp. 436–444.

[83] A. C. LIN, A. M. BYGRAVE, A. DE CALIGNON, T. LEE, AND G. MIESENBOCK, *Sparse, decorrelated odor coding in the mushroom body enhances learned odor discrimination*, *Nat. Neurosci.*, 17 (2014), pp. 559–568.

[84] S. X. LUO, R. AXEL, AND L. F. ABBOTT, *Generating sparse and selective third-order responses in the olfactory system of the fly*, Proc. Natl. Acad. Sci. USA, 107 (2010), pp. 10713–10718.

[85] S. MARCELJA, *Mathematical description of the responses of simple cortical cells*, J Opt Soc Am, 70 (1980), pp. 1297–1300.

[86] A. MARESH, D. RODRIGUEZ GIL, M. C. WHITMAN, AND C. A. GREER, *Principles of glomerular organization in the human olfactory bulb—implications for odor processing*, PLoS One, 3 (2008), p. e2640.

[87] H. MARKRAM, J. LUBKE, M. FROTSCHER, A. ROTH, AND B. SAKMANN, *Physiology and anatomy of synaptic connections between thick tufted pyramidal neurones in the developing rat neocortex*, J. Physiol., 500 (Pt 2) (1997), pp. 409–440.

[88] W. MATHER, M. R. BENNETT, J. HASTY, AND L. S. TSIMRING, *Delay-induced degrade-and-fire oscillations in small genetic circuits*, Phys. Rev. Lett., 102 (2009), p. 068105.

[89] D. MC LAUGHLIN, R. SHAPLEY, M. SHELLEY, AND D. J. WIELAARD, *A neuronal network model of macaque primary visual cortex (v1): Orientation selectivity and dynamics in the input layer 4Ca*, Proceedings of the National Academy of Sciences, 97 (2000), pp. 8087–8092, <https://doi.org/10.1073/pnas.110135097>.

[90] D. MC LAUGHLIN, R. SHAPLEY, M. SHELLEY, AND J. WIELAARD, *A neuronal network model of macaque primary visual cortex (V1): Orientation selectivity and dynamics in the input layer 4Ca*, Proc. Natl. Acad. Sci. USA, 97 (2000), pp. 8087–8092.

[91] R. E. MIROLLO AND S. H. STROGATZ, *Synchronization of pulse-coupled biological oscillators*, SIAM Journal on Applied Mathematics, 50 (1990), pp. 1645–1662.

[92] K. MORI, H. NAGAO, AND Y. YOSHIHARA, *The olfactory bulb: coding and processing of odor molecule information*, Science, 286 (1999), pp. 711–715.

[93] C. M. NIELL, *Cell types, circuits, and receptive fields in the mouse visual cortex*, Annu. Rev. Neurosci., 38 (2015), pp. 413–431.

[94] A. M. PACKER, L. E. RUSSELL, H. W. DALGLEISH, AND M. HAUSSER, *Simultaneous all-optical manipulation and recording of neural circuit activity with cellular resolution in vivo*, Nat. Methods, 12 (2015), pp. 140–146.

[95] X. PITKOW AND M. MEISTER, *Decorrelation and efficient coding by retinal ganglion cells*, Nat. Neurosci., 15 (2012), pp. 628–635.

[96] A. RAUCH, G. LA CAMERA, H. LUSCHER, W. SENN, AND S. FUSI, *Neocortical pyramidal cells respond as integrate-and-fire neurons to in vivo-like input currents*, J Neurophysiol, 90 (2003), pp. 1598–1612, <https://doi.org/10.1152/jn.00293.2003>.

[97] J. P. RICKGAUER, K. DEISSEROTH, AND D. W. TANK, *Simultaneous cellular-resolution optical perturbation and imaging of place cell firing fields*, Nat. Neurosci., 17 (2014), pp. 1816–1824.

[98] A. ROXIN, H. RIECKE, AND S. SOLLA, *Self-sustained activity in a small-world network of excitable neurons*, Phys. Rev. Lett., 92 (2004), p. 198101, <https://doi.org/10.1103/PhysRevLett.92.198101>.

[99] M. P. SCENIAK, D. L. RINGACH, M. J. HAWKEN, AND R. SHAPLEY, *Contrast's effect on spatial summation by macaque V1 neurons*, Nat. Neurosci., 2 (1999), pp. 733–739.

[100] C. E. SHANNON, *Communication in the Presence of Noise*, Proceedings of the IRE, 37 (1949), pp. 10–21.

[101] D. SOMERS, S. NELSON, AND M. SUR, *An emergent model of orientation selectivity in cat visual cortical simple cells*, Journal of Neuroscience, 15 (1995), pp. 5448–5465.

[102] D. L. SOSULSKI, M. L. BLOOM, T. CUTFORTH, R. AXEL, AND S. DATTA, *Distinct representations of olfactory information in different cortical centres*, Nature, 472 (2011), p. 213–216, <https://doi.org/10.1038/nature09868>, <https://europepmc.org/articles/PMC3354569>.

[103] P. D. SPEAR, C. B. KIM, A. AHMAD, AND B. W. TOM, *Relationship between numbers of retinal ganglion cells and lateral geniculate neurons in the rhesus monkey*, Vis. Neurosci., 13 (1996), pp. 199–203.

[104] O. SPORNS AND C. HONEY, *Small worlds inside big brains*, Proc Natl Acad Sci U S A, 103 (2006), pp. 19219–19220, <https://doi.org/10.1073/pnas.0609523103>.

[105] P. STERLING AND S. LAUGHLIN, *Principles of Neural Design*, 06 2015, <https://doi.org/10.7551/mitpress/9780262028707.001.0001>.

[106] O. STETTER, D. BATTAGLIA, J. SORIANO, AND T. GEISEL, *Model-free reconstruction of excitatory neuronal connectivity from calcium imaging signals*, PLoS Comput. Biol., 8 (2012), p. e1002653.

[107] I. H. STEVENSON, J. M. REBESCO, L. E. MILLER, AND K. P. KORDING, *Inferring functional connections between neurons*, Curr. Opin. Neurobiol., 18 (2008), pp. 582–588.

1014 [108] W. B. THORESON, *Kinetics of synaptic transmission at ribbon synapses of rods and cones.*,
1015 Mol Neurobiol, 36 (2007), pp. 205–223, <https://doi.org/10.1007/s12035-007-0019-9>.

1016 [109] S. TRENHOLM, D. J. SCHWAB, V. BALASUBRAMANIAN, AND G. B. AWATRAMANI, *Lag normalization*
1017 *in an electrically coupled neural network*, Nat. Neurosci., 16 (2013), pp. 154–156,
1018 <https://doi.org/10.1038/nn.3308>.

1019 [110] A. TREVES, *Mean field analysis of neuronal spike dynamics*, Network, 4 (1993), pp. 259–284.

1020 [111] P. K. TRONG AND F. RIEKE, *Origin of correlated activity between parasol retinal ganglion*
1021 *cells*, Nat. Neurosci., 11 (2008), pp. 1343–1351.

1022 [112] J. A. TROPP AND A. C. GILBERT, *Signal Recovery From Random Measurements Via Orthogonal*
1023 *Matching Pursuit*, IEEE Trans. Inform. Theory, 53 (2007), pp. 4655–4666.

1024 [113] T. W. TROYER AND K. D. MILLER, *Physiological gain leads to high ISI variability in a simple*
1025 *model of a cortical regular spiking cell*, Neural Comput, 9 (1997), pp. 971–983.

1026 [114] G. C. TURNER, M. BAZHENOV, AND G. LAURENT, *Olfactory representations by Drosophila*
1027 *mushroom body neurons*, J. Neurophysiol., 99 (2008), pp. 734–746.

1028 [115] M. VAN DEN HEUVEL, C. STAM, M. BOERSMA, AND H. HULSHOFF POL, *Small-world and scale-*
1029 *free organization of voxel-based resting-state functional connectivity in the human brain.*,
1030 Neuroimage, 43 (2008), pp. 528–539, <https://doi.org/10.1016/j.neuroimage.2008.08.010>.

1031 [116] C. VAN VREESWIJK AND H. SOMPOLINSKY, *Chaos in neuronal networks with balanced excitatory*
1032 *and inhibitory activity*, Science, 274 (1996), pp. 1724–1726.

1033 [117] X. J. WANG, *Calcium coding and adaptive temporal computation in cortical pyramidal neu-*
1034 *rons*, J. Neurophysiol., 79 (1998), pp. 1549–1566.

1035 [118] C. WELKER, *Receptive fields of barrels in the somatosensory neocortex of the rat*, J. Comp.
1036 Neurol., 166 (1976), pp. 173–189.

1037 [119] G. WERNER AND V. B. MOUNTCASTLE, *Neural activity in mechanoreceptive cutaneous af-*
1038 *ferents: Stimulus-response relations, Weber functions, and information transmission*, J.
1039 Neurophysiol., 28 (1965), pp. 359–397.

1040 [120] T. N. WIESEL, *Receptive fields of ganglion cells in the cat's retina*, J Physiol, 153 (1960),
1041 pp. 583–594.

1042 [121] D. A. WILSON, *Receptive fields in the rat piriform cortex*, Chem. Senses, 26 (2001), pp. 577–
1043 584.

1044 [122] A. WOHRER AND P. KORNPROBST, *Virtual retina: a biological retina model and simulator,*
1045 *with contrast gain control.*, J Comput Neurosci, 26 (2009), pp. 219–249, <https://doi.org/10.1007/s10827-008-0108-4>.

1046 [123] C. YU, K. PROKOP-PRIGGE, L. WARRENBURG, AND J. MAINLAND, *Drawing the borders of*
1047 *olfactory space*, in Chemical Senses, vol. 40, OXFORD UNIV PRESS GREAT CLAREN-
1048 DON ST, OXFORD OX2 6DP, ENGLAND, 2015, pp. 565–565.

1049 [124] L. ZHAOPENG, *A new framework for understanding vision from the perspective of the primary*
1050 *visual cortex*, Curr. Opin. Neurobiol., 58 (2019), pp. 1–10.

1051 [125] D. ZHOU, Y. XIAO, Y. ZHANG, Z. XU, AND D. CAI, *Causal and structural connectivity of*
1052 *pulse-coupled nonlinear networks*, Phys. Rev. Lett., 111 (2013), p. 054102.

1053